Degenerate nucleation in the Cahn-Hilliard-Cook model

Dirk Blömker, Evelyn Sander, Thomas Wanner

Angaben zur Veröffentlichung / Publication details:

Blömker, Dirk, Evelyn Sander, and Thomas Wanner. 2016. "Degenerate nucleation in the Cahn-Hilliard-Cook model." *SIAM Journal on Applied Dynamical Systems* 15 (1): 459–94. https://doi.org/10.1137/15m1028844.

SIAM J. Applied Dynamical Systems
Vol. 15, No. 1, pp. 459–494

Degenerate Nucleation in the Cahn–Hilliard–Cook Model*

Dirk Blömker†, Evelyn Sander‡, and Thomas Wanner‡

Abstract. Phase separation in metal alloys is an important pattern forming physical process with applications in materials science, both for understanding materials structure and for the design of new materials. The Cahn–Hilliard equation is a deterministic model for the dynamics of alloys which has proven to be fundamental for the understanding of several types of phase separation behavior. However, stochastic effects occur in any physical experiment and thus need to be incorporated into models. While white noise is one standardly chosen option, it is not immediately clear in which way the noise characteristics affect the resulting patterns. In this paper we study the effects of not necessarily small colored noise on pattern formation in a stochastic Cahn–Hilliard model in the nucleation regime. More precisely, we focus on degenerate noise which acts either on isolated eigenmodes or with a well-defined spatial wavelength. Our studies show that the types of resulting patterns depend critically on the spatial noise frequency, and we can explain via numerical continuation methods that if this spatial frequency is too high, then pattern formation is significantly impaired by the underlying structure of the system. In addition, we provide rigorous bounds on the nucleation time frame in the degenerate stochastic setting.

Key words. Cahn–Hilliard–Cook systems, nucleation, stochastic partial differential equation, domain exit, degenerate noise, pattern formation

AMS subject classifications. 35B40, 35B41, 35K55, 60F10, 60H15, 74N99

DOI. 10.1137/15M1028844

1. Introduction.

Phase separation in metal alloys gives rise to many interesting and intriguing pattern formation phenomena, and understanding such patterns is of practical interest in the design of new materials. If a mixture of metallic components is heated to a sufficiently high temperature, stirred to form a homogeneous mixture, and subsequently quenched, then several types of phase separation can occur. In this paper, we consider a specific phase separation process called nucleation in binary alloys, which occurs when the alloy consists predominantly of one element with significantly smaller amounts of a second one. In this case, small droplets are observed to form within the mixture; see Figure 1. Although these droplets form at random positions, they have a characteristic size, shape, composition, and spacing. In this paper, we study a stochastic Cahn–Hilliard model of nucleation. Previous studies have used space-time white noise in this equation, and in this case, large deviation

*Received by the editors July 2, 2015; accepted for publication (in revised form) December 16, 2015; published electronically February 25, 2016. This research was supported in part by the Institute for Mathematics and Its Applications at the University of Minnesota with funds provided by the National Science Foundation.
http://www.siam.org/journals/siads/15-1/M102884.html
†Institut für Mathematik, Universität Augsburg, 86135 Augsburg, Germany (dirk.bloemker@math.uni-augsburg.de).
‡Department of Mathematical Sciences, George Mason University, Fairfax, VA 22030 (esander@gmu.edu, twanner@gmu.edu). The work of the second and third authors was partially supported by NSF grants DMS-0639300, DMS-0907818, and DMS-1407087. In addition, the work of the third author was partially supported by NSF grant DMS-1114923.

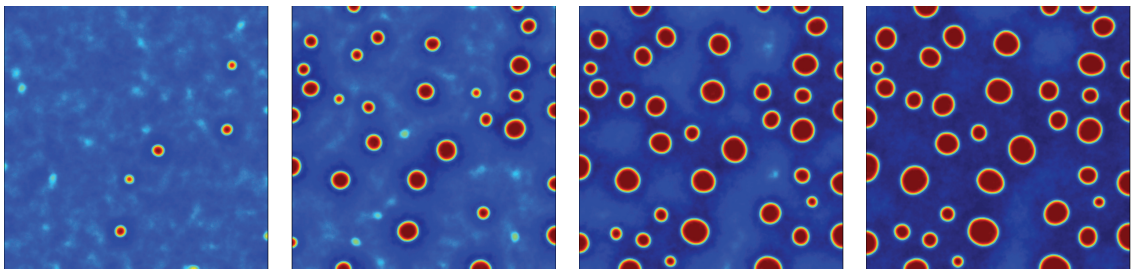

Figure 1. *Nucleation in the Cahn–Hilliard–Cook equation with white noise forcing. The images show snapshots of a solution which originates at the homogeneous state $\mu = -0.59$, and we choose $\varepsilon = 0.005$ as well as $\sigma = 0.050$. From left to right the depicted solutions are for times $t = 0.00265 \cdot k$ for $k = 1, \dots, 4$.*

results give rigorous bounds on the time to nucleation and pattern formation at nucleation [2] at least in the small noise regime. In contrast, we concentrate on how the nature of the noise affects the droplet size. In particular, we use degenerate noise which acts only on one or on a small collection of modes with specific frequencies. Even though the large deviations results no longer apply in this situation, one still expects nucleation to occur almost surely, and we are in fact able to obtain lower bounds on the nucleation time frame. We also demonstrate that depending on the spatial frequency of the noise, the observed nucleation patterns may occur at completely different wavelengths due to an inherent maximal droplet count which can be supported on a given domain size.

Cahn and Hilliard derived a fourth order partial differential equation to serve as a phenomenological model for phase separation in binary alloys, written here in dimensionless form as

$$\begin{aligned} u_t &= -\Delta(\varepsilon^2 \Delta u + f(u)) \quad \text{in} \quad \Omega\,, \\ &\frac{\partial u}{\partial \nu} = \frac{\partial \Delta u}{\partial \nu} = 0 \quad \text{on} \quad \partial\Omega\,. \end{aligned} \tag{1.1}$$

In this formulation, the function u is an order parameter; i.e., it is basically the difference of the concentrations of the two alloy components as a function of time and space. Thus, u-values close to -1 and 1 correspond to the two pure material components, and values in between correspond to mixtures, with zero representing equal concentrations of both components. The constant $\varepsilon > 0$ is a small dimensionless quantity modeling interaction length. The domain $\Omega \subset \mathbb{R}^d$ is bounded with appropriately smooth boundary for $d \in \{1, 2, 3\}$, and the nonlinearity in the equation is given by $f(u) = u - u^3$, implying that $-f$ is the derivative of the standard double-well potential $F(u) = (u^2 - 1)^2/4$. The Cahn–Hilliard equation generates gradient-like dynamics with respect to the van der Waals free energy functional [34]

$$E_\varepsilon[u] = \int_\Omega \left(\frac{\varepsilon^2}{2} |\nabla u|^2 + F(u) \right) dx\,. \tag{1.2}$$

In addition, it conserves the total mass $\int_\Omega u\, dx$, and for later reference we define the average mass μ via

$$\mu = \frac{1}{|\Omega|} \int_\Omega u\, dx\,, \qquad \text{where we set} \qquad |\Omega| = \int_\Omega 1\, dx\,.$$

It is immediate that the constant function $u(t,x) \equiv \mu$ is a solution to the Cahn–Hilliard equation which corresponds to a perfectly homogeneous mixture in the experiments. We focus on solutions with initial conditions which are close to but different from this homogeneous state, as generated, for example, by unavoidable small fluctuations before the quenching process. If we define the monotone increasing sequence $(\kappa_k)_{k\in\mathbb{N}}$ as the, strictly positive, eigenvalues of the negative Laplacian $-\Delta$ subject to Neumann boundary conditions and zero mass constraint, then one can show as in [31, 32] that the eigenvalues of the linearized Cahn–Hilliard equation at the homogeneous equilibrium μ are given by

$$\eta_{k,\varepsilon} = \kappa_k(f'(\mu) - \varepsilon^2\kappa_k) \quad \text{for} \quad k \in \mathbb{N}\,, \tag{1.3}$$

where we restrict the dynamics of (1.1) to functions with spatial average μ. Therefore, the homogeneous equilibrium μ is unstable when ε is sufficiently small and $-1/\sqrt{3} < \mu < 1/\sqrt{3}$. This set of mass values is typically known as the *spinodal region*, and the associated phase separation mechanism is called *spinodal decomposition* [26, 27, 32, 36]. On the other hand, the homogeneous equilibrium is asymptotically stable for mass values μ with $f'(\mu) = 1 - 3\mu^2 < 0$, i.e., for $\mu > 1/\sqrt{3}$ or $\mu < -1/\sqrt{3}$. Notice also that by symmetry the negative mass case is identical to the positive mass case, since one only has to consider $-u$ instead of u. The latter mass condition defines the so-called *nucleation region* or *metastable region* of parameter space.

In their seminal paper, Bates and Fife [1] showed that if the total mass μ is in the nucleation regime for the deterministic Cahn–Hilliard equation on one-dimensional base domains Ω, and if the homogeneous equilibrium is perturbed in the right direction by a sufficiently large amount, then the solution originating at the perturbed state will no longer relax to the homogeneous equilibrium but will rather converge to a lower energy state which exhibits phase separation. Notice, however, that due to the asymptotic stability of the homogeneous state μ, small perturbations lead to solutions which converge to μ and therefore do not exhibit phase separation at all. In other words, the Cahn–Hilliard model (1.1) cannot explain the initial dynamics of nucleation, as it cannot intrinsically introduce the necessary perturbation of the initial state.

Thus, in order to study the statistical properties of the initial dynamics of nucleation, it is necessary to consider a stochastic model. In this paper, we use the stochastic extension of the Cahn–Hilliard model due to Cook [8] and Langer [23], which incorporates additive random thermal fluctuations into (1.1). The resulting Cahn–Hilliard–Cook equation is also known as "Model B" in the classification of Hohenberg and Halperin [20], and it is given by

$$\begin{aligned} u_t &= -\Delta(\varepsilon^2\Delta u + f(u)) + \sigma\cdot\xi \quad \text{in} \quad \Omega\,, \\ &\frac{\partial u}{\partial \nu} = \frac{\partial \Delta u}{\partial \nu} = 0 \quad \text{on} \quad \partial\Omega\,. \end{aligned} \tag{1.4}$$

In this formulation, the additive noise term ξ is usually chosen as a mass-conserving space-time white noise or colored noise, and the parameter σ is a measure for the intensity of the noise. For more details, see, for example, [4, 5, 6].

For sufficiently small noise intensity, it was shown in [2] that solution paths of the stochastic Cahn–Hilliard–Cook model (1.4) which originate near the homogeneous state $\bar{u} \equiv \mu$ will exit its deterministic domain of attraction with probability one, and at the time of exit these paths

will be close to the boundary spikes which were identified in [1]. The behavior explains the development of the minimal perturbations mentioned above. Reference [11] studied a variation of this model for multicomponent alloys on two-dimensional base domains, showing that the number of droplets and droplet type could be understood using a combination of scaling laws and numerical continuation.

Both of the above studies considered essentially nondegenerate noise. But how do degeneracies in the noise affect the pattern formation process? For example, what happens if the noise forcing term ξ is limited to a fixed band of noise frequencies or, in the extreme case, to just one eigenmode of the Laplacian? We would like to point out that in this situation, classical Freidlin–Wentzell-type results based on large deviations can no longer be applied. Nevertheless, one would still expect the existence of a unique ergodic invariant measure which is supported everywhere. In fact, this should be a straightforward but nontrivial modification of the work by Hairer and Mattingly [17, 18], and it would imply that even under degenerate noise nucleation will occur at some point with probability one. This approach is partly carried out in [15].

In the present paper, we perform a combined numerical and theoretical study in order to shed light on nucleation phenomena in the degenerate noise setting. In section 2 we perform simulations for noise terms restricted to bands of frequencies of a variety of radii. We find that droplets form in four possible ways:

- For small radius bands, droplets are oddly shaped.
- For medium radius bands, droplets form in a semiregular grid pattern, with droplet numbers varying quadratically as a function of the radius.
- For large radius bands, the droplets take longer to form or fail to form in the expected patterns, with an overrepresentation of boundary and corner droplets compared to the nondegenerate case.
- For a sufficiently large spatial frequency noise forcing band, we do not observe droplet formation in our simulations, even for relatively large noise strength.

Our results are further supported by simulations in which only one single spatial noise frequency is excited. In section 3, we explain the results of the direct simulations by using numerical equilibrium continuation for the underlying deterministic system. In particular, we restrict our focus to a small portion of the domain, sustaining only a small number of droplets. Via numerical continuation we show that if the domain is too small, it is not possible for a droplet to form, or, equivalently, there is a maximum droplet count for a given domain size. In addition to explaining the observations of the direct simulations, these results also uncover a remarkable scaling invariance in the equilibrium bifurcation diagram and demonstrate that path-following for small domains suffices to explain the nucleation behavior on large domains. In section 4, we derive rigorous stochastic estimates which imply that although our degenerate noise situation precludes the use of large deviations techniques, one can still obtain bounds on the time frame necessary for nucleation. The paper closes with conclusions and future directions in section 5.

2. Degenerate noise simulations.

In this section we present numerical simulations of the Cahn–Hilliard–Cook equation (1.4) subject to homogeneous Neumann boundary conditions and driven by degenerate noise. In order to develop some intuition for the effects of this

kind of noise, we focus on two specific degeneracies. In section 2.1 we consider band-limited noise, meaning noise which only acts on Fourier modes whose wave vectors lie in a specified annulus. In section 2.2 we consider the case of single mode forcing. Our numerical methods are described briefly in section 2.3.

2.1. Band-limited simulations. In order to specify the degeneracy of the noise perturbation considered, we recall that the noise process $\xi = \partial_t W$ in (1.4) is given by the generalized derivative of a Q-Wiener process W as defined in [10], which can be written as a Fourier series of the form

$$W(t) = \sum_{j,k=0}^{\infty} a_{j,k}\, \beta_{j,k}(t) \cos(k\pi x) \cos(j\pi y) \qquad \text{with} \qquad a_{0,0} = 0\,, \tag{2.1}$$

where $\{\beta_{j,k}\}_{j,k\in\mathbb{N}_0}$ denotes a family of independent real-valued standard Brownian motions, and the numbers $\{a_{j,k}\}_{j,k\in\mathbb{N}_0}$ are given weights with $a_{0,0} = 0$. Note that the latter assumption ensures that the noise process ξ in (1.4) preserves the total mass $\int_\Omega u\,dx$. The use of the cosine basis is due to the fact that the Cahn–Hilliard–Cook model uses homogeneous Neumann boundary conditions. In general, for other types of series we cannot easily localize the noise in Fourier space.

By imposing additional constraints on the weights $a_{j,k}$ in (2.1) we can now consider different noise processes in (1.4). In the present section, we perform simulations with *band-limited noise*, which is defined as follows. Consider two radii $0 \le r_0 < r_1$; then we define

$$a_{j,k} = \begin{cases} 1 & \text{for } \ r_0 < |(j,k)| < r_1\,, \\ 0 & \text{otherwise}\,, \end{cases}$$

where we use $|(j,k)| = (j^2 + k^2)^{1/2}$ as an abbreviation for the norm of the wave vector.

For the remainder of section 2.1, we concentrate on the effect of the choice of r_0 on the total droplet count observed during nucleation in (1.4). Note that if the difference $r_1 - r_0$ is fixed, then the total number of modes which are excited by noise increases with r_0. However, we do not find that this larger number of modes produces the most dominant effect, and we therefore keep $r_1 - r_0$ fixed in each set of simulations. Moreover, the analytic results of section 4 actually show that in two dimensions the effect of taking $r_1 - r_0$ as fixed, and thus increasing the number of modes for large r_0, is balanced by the stronger linear damping for larger wave numbers. The two effects do not cancel, but in the range of r_0-values which we consider the impact is not significant.

We now turn our attention to presenting and analyzing our simulations of (1.4) driven by band-limited noise. In each case, the simulation begins at the homogeneous state $u \equiv \mu$ at time $t = 0$, and the solution snapshot is shown at a small fixed time t_{max}. Note that for such simulations of the Cahn–Hilliard–Cook equation, under both degenerate and nondegenerate noise forcing, there are no droplets at time $t = 0$. If the noise is sufficiently large, then over a relatively short time nucleation occurs; i.e., the number of droplets increases. Once the nucleation stage is completed, the dynamics transitions to a coarsening regime, during which the droplets disappear or merge and the total droplet count decreases again. We refer to nucleation and coarsening as two disjoint regimes. In fact, both dynamical behaviors are

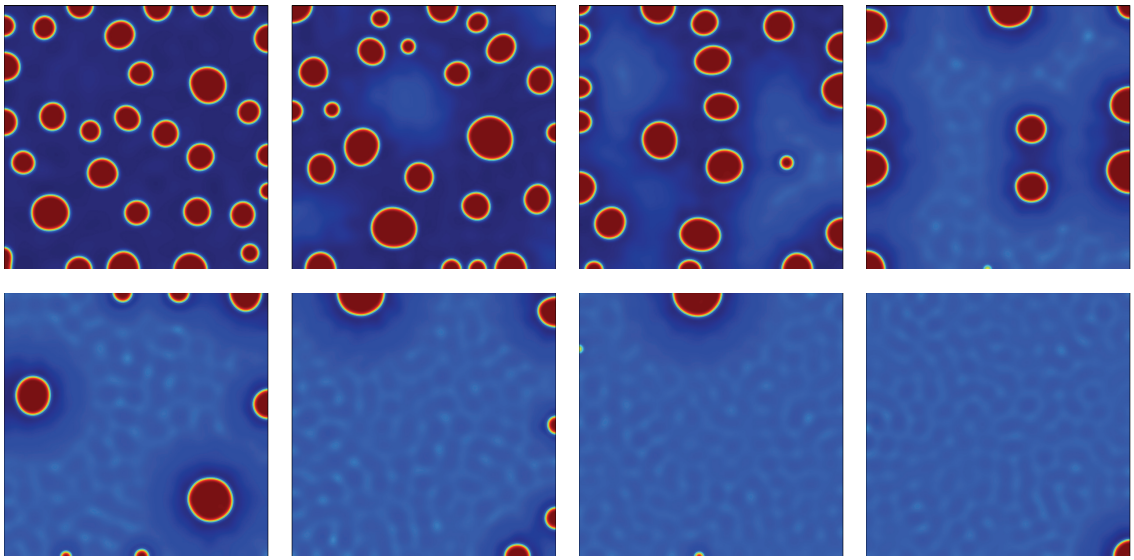

Figure 2. *Simulations for the Cahn–Hilliard–Cook equation with band-limited noise with frequencies in the range* (r_0, r_1)*. From left to right, starting at the upper left, the images are for* $r_0 = 10, 15, 16, 17, 18, 19, 20, 21$*, and in all cases we choose* $r_1 = r_0 + 10$*. In each simulation, the solution originates at the homogeneous state* $\mu = -0.59$ *for* $t = 0$*, and each figure shows the resulting solution at time* $t = 0.025478$*. Red and blue correspond to* $u = 1$ *and* $u = -1$*, respectively, the pure concentrations of the two metallic components, with intermediate colors corresponding to mixtures of the metallic components. In all cases, the noise intensity is* $\sigma = 0.05$*, and the interaction length is chosen as* $\varepsilon = 0.005$*. The total number of excited spatial noise frequency modes is given by* 249*,* 327*,* 343*,* 361*,* 373*,* 387*,* 405*, and* 419*, respectively.*

present at varying degrees at all times, but we have observed that, aside from a quite small time window, one behavior significantly dominates the other. Namely, once a nucleus is fully formed, the phase separation effectively saturates the domain and prevents any nearby formation of new nuclei. In future work, we plan to do a more detailed study of this saturation effect. In this paper, we are interested in the effect of degenerate noise on the initial nucleation regime, and in particular in the associated pattern selection, which is why we have chosen to depict the solutions when t_{max} is relatively small.

Our first set of simulation results is shown in Figure 2, and we refer the reader to section 2.3 for a description of our numerical methods. The eight images in the figure depict solution snapshots as described in the previous paragraph, with band-limited noise for increasing values of r_0 from top left to bottom right. In each case, we set $r_1 = r_0 + 10$, allow the simulations to originate at the homogeneous state $u \equiv \mu = -0.59$, and show the solution at time $t_{max} = 0.025478$. The images clearly indicate a change in the solution behavior depending on r_0. In particular, in Figure 2 a smaller value of r_0 corresponds to a larger number of droplets. Does nucleation just occur more quickly for these smaller r_0-values? In each case, we ran the simulations over a longer time frame, and these longer-term simulations show that this is in fact not the case. Specifically, running the simulations up to time $t_{max} = 0.05$, one can observe that for larger r_0 fewer droplets form before the simulation enters the coarsening regime. In all cases we have confirmed that the time value $t = 0.05$ lies beyond the time exhibiting the maximal droplet count. We would like to point out that the observed change in maximal

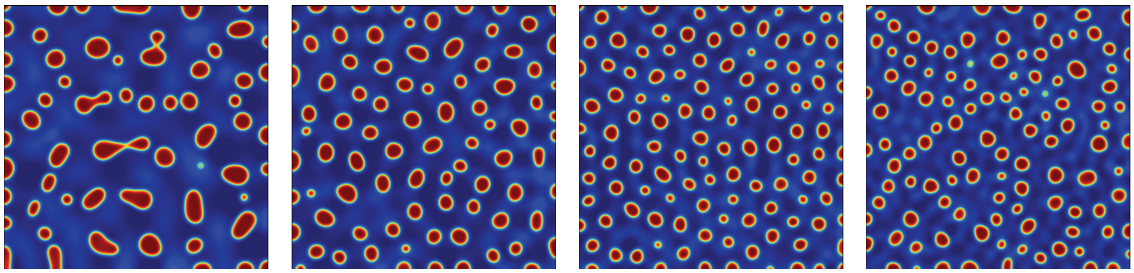

Figure 3. *Simulations for the Cahn–Hilliard–Cook equation with a narrow band of noise frequencies in the range* $(r_0, r_1) = (n - 0.5, n + 0.5)$ *for a number of integer values* n*. From left to right, the images correspond to* $n = 11, 17, 23, 29$*. In each simulation, the solution originates at the homogeneous state* $\mu = -0.59$*, and each image shows the resulting solution at time* $t = 0.005096$*. The noise intensity is chosen as* $\sigma = 1.0$*, and the interaction length is again* $\varepsilon = 0.005$*. For the four simulations, the total number of excited spatial noise frequency modes is given by* 19*,* 29*,* 37*, and* 44*, respectively.*

droplet counts is not negligible. In three different simulations with $r_0 = 10$, the maximum droplet count varies, but it is always in the 30's. For $r_0 = 15$ and $r_0 = 16$, the maximum droplet count is closer to 20, while for $r_0 = 17, 18, 19$ the numbers are around 10. Finally, for $r_0 = 20$ and $r_0 = 21$ the maximal droplet count drops to usually either one or zero. In all our simulations with r_0-values $21 < r_0 < 40$, not a single droplet nucleated up to time $t_{max} = 0.05$. In these cases, we only expect nucleation due to large deviations type effects on a much longer time-scale. As a final comment, we would like to point out that aside from the change in droplet count, the simulations in Figure 2 also indicate an interesting change in droplet configuration. For larger values of r_0, droplets appear primarily at the boundary or in the corners of the domain.

In order to better understand the effect of changes in r_0 on the droplet count, we now make the band of noise frequencies much narrower by choosing $(r_0, r_1) = (n - 0.5, n + 0.5)$ for integer values n. The resulting simulations are shown in Figure 3. Notice that the number of excited modes is now smaller by a factor of around $1/20$ than in the case of large band simulations. In order to still observe nucleation on a small time frame, we have therefore increased the noise intensity by a factor of 20 to $\sigma = 1.0$. One can see that now the pattern formation occurs much sooner than in the large band situation. Moreover, the images in Figure 3 indicate that for small values of n, roughly up to the case $n = 11$ in the leftmost image, droplets are oddly shaped. For midrange values of r_0, starting at around $n = 12$, droplets form on an almost uniform grid. However, for larger values such as $n = 44$, there appear to be some missing droplets in the grid which never get resolved. Furthermore, for sufficiently large values of r_0, which are not shown in the figure, we observe the same effect as in the large band case $r_1 - r_0 = 10$ discussed above: The droplet number decreases, the droplets become clustered at the boundaries and corners, and finally the droplets cease to form within the considered simulation time frame.

While the above simulations provide some qualitative intuition, a more quantitative description seems to be in order. For this, we perform a much larger number of simulations in a variety of settings and compare the obtained average droplet counts. The results of these simulations are contained in Figure 4. In this figure, the average droplet count data is based

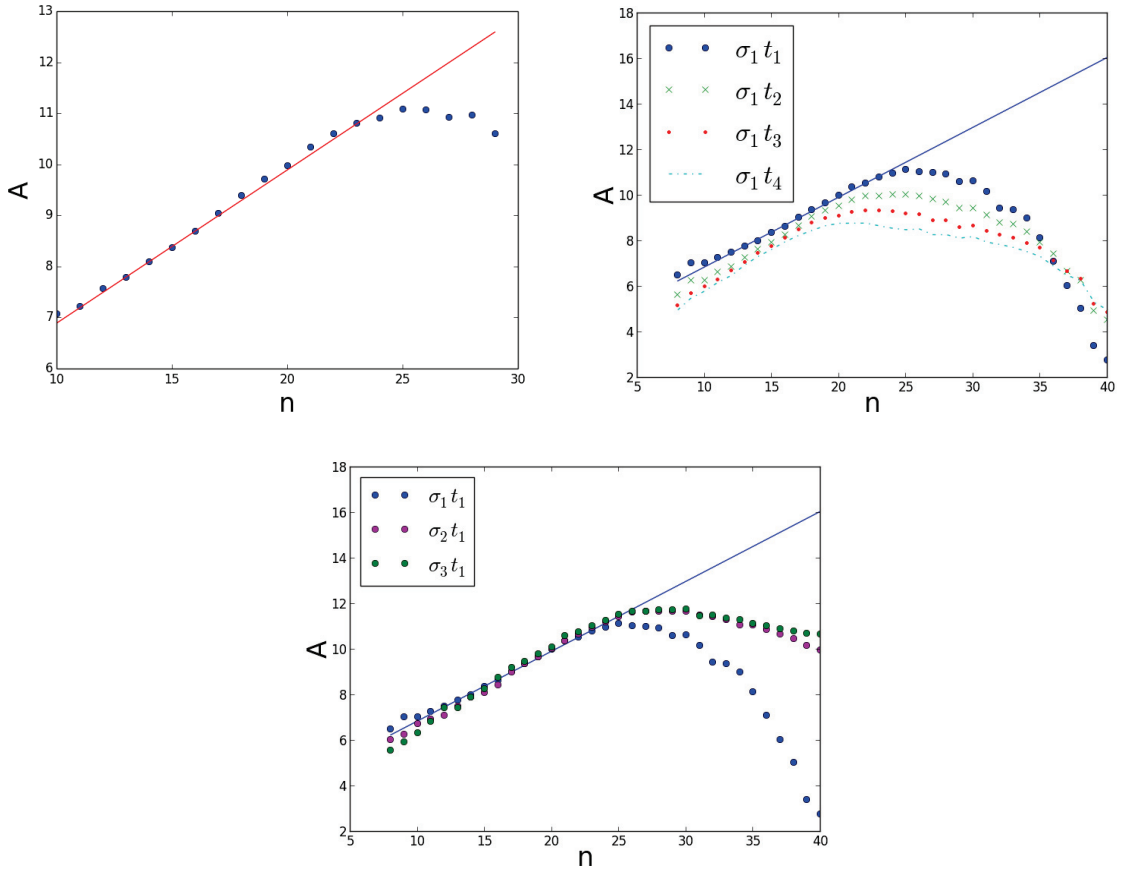

Figure 4. *The top left image shows a plot of A, which denotes the square root of the mean number of droplets, versus n, where the excited noise frequencies are contained in a narrow band of the form $(r_0, r_1) = (n-0.5, n+0.5)$. The plot shows data for $n = 10, \ldots, 29$. For each averaged data point, we performed $M = 100$ runs using the same parameters as in Figure 3. In particular, each simulation uses noise intensity $\sigma = 1.0$ and ends at time $t = 0.005096$. The red fit line was determined by using only the data points at $n = 11, \ldots, 20$. The top right image depicts A versus n for $n = 8, \ldots, 40$, but now at the times $t_k = 0.005096 \cdot k$, where we consider $k = 1, 2, 3, 4$. In this situation, the values of A decrease at larger times due to coarsening. For each data point, we now performed $M = 20$ simulations. Finally, the bottom image shows A as a function of n for $n = 8, \ldots, 40$ at $t_1 = 0.005096$ and for noise intensities $\sigma_\ell = \ell$, where $\ell = 1, 2, 3$. Also, in this case, $M = 20$ simulations were performed for each data point. One can see that a larger noise intensity results in quicker nucleation.*

on M simulations and for a range of n-values. In each graph, the vertical axis corresponds to the square root of the mean number of droplets at a fixed time value t, and we denote this quantity by A. This choice of quantity is clearly motivated by the almost grid-like patterns which were observed in the two center panels of Figure 3.

We first turn our attention to the top left panel in Figure 4, which uses $M = 100$ simulations for each data point. It shows a plot of A as a function of the band center $n = 10, \ldots, 29$, which indicates that A grows almost linearly for $10 \leq n \leq 23$. The red line in the image is a linear fit for the data points $11 \leq n \leq 20$, which turns out to be a good fit up to $n = 23$. However, starting at $n = 24$, the values A no longer change linearly. This is caused by the

onset of the nucleation failure which we observed in the wide spatial frequency band simulations in Figure 2. This effect becomes progressively more pronounced as n grows, such that by $n = 40$, the droplets almost exclusively form on the boundary, and by $n = 45$ no droplets form at all during the considered time frame.

In order to rule out insufficient simulation time or insufficient noise intensity as explanations for this nucleation failure, we performed simulations up to double, triple, and quadruple times, as well as for double and triple noise intensities. The results from these simulations are shown in the top right and bottom panels in Figure 3, and they use $M = 20$ simulations for each data point. They indicate that larger simulation time frames lead to a decrease in droplet counts due to the onset of coarsening. Furthermore, higher noise intensities allow the dynamics to reach the maximal droplet count earlier, and the droplet counts for larger values of n are increased. Nevertheless, in all simulations the deviation from the linear growth regime for A occurs at around $n = 23$.

Our simulations indicate somewhat similar behavior for the wide band case $r_1 - r_0 = 10$ and for the narrow band case $r_1 - r_0 = 1$. For small values of the parameter r_0, the droplets appear fairly regularly spaced in the interior and on the boundary and corners of the domain. For larger values of r_0, droplets first fail to form at some of the grid points, and then are only created along the boundary of the underlying domain Ω. Finally, if the value of r_0 is sufficiently large, nucleation cannot be observed over the time frames used in our simulations. We now summarize the findings of the numerics in this section.

Observation 2.1. For band-limited noise, a large band and a narrow band of excited frequencies behave similarly, but this behavior depends significantly on the spatial frequency of the band. A small spatial frequency band quickly gives rise to patterns of irregular droplet shapes, but with a geometry based on the noise excitation. A medium spatial frequency band gives rise to regularly shaped droplets in a geometry based on the noise excitation. A large spatial frequency band takes longer to invoke droplets, these droplets do not fully conform to the geometry of the excited noise patterns, and the droplets occur with over-representation on the boundary and in the corners. Even larger spatial frequency noise does not invoke any nucleating patterns in the time frame of our simulations.

2.2. Single forcing mode simulations. We now turn our attention to even more degenerate noise. While in the last section the noise acted on modes whose wave numbers fell into specific intervals, this section is devoted to noise which acts on exactly one mode. As before, we study the expected droplet count that can be generated in this way. Intuitively, we would again anticipate that the droplet count rises as the wave number of the considered mode increases, since higher frequencies correspond to a larger number and smaller size of the connected components of the positive nodal domain of the mode. In particular, consider the case of stochastic forcing which acts only on the (j, k)-mode given by

$$\varphi_{j,k}(x, y) = \cos(j\pi x)\cos(k\pi y)\ , \tag{2.2}$$

which has frequencies $j/2$ and $k/2$ with respect to the x- and the y-directions, respectively. For each of these functions $\varphi_{j,k}(x, y)$, their two nodal domains, i.e., the sets where the function is strictly positive or strictly negative, respectively, decompose into a specific number of components, as shown, for example, in Figure 5. From left to right, the image contains

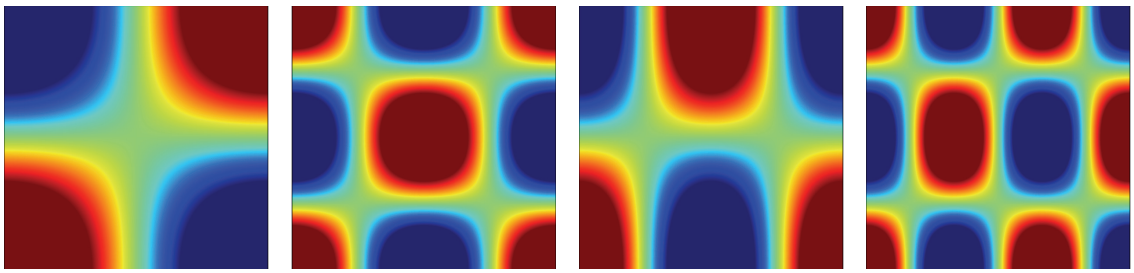

Figure 5. *Nodal domain patterns of the (j,k)-modes $\varphi_{j,k}$ defined in (2.2). From left to right, the images are for $(j,k) = (1,1)$, $(2,2)$, $(2,1)$, and $(3,2)$. In each image, positive function values correspond to red, negative ones to blue, and green is for the value zero. If these modes are forced by noise, one would expect to see the nucleation of $1/2$, 2, 1, and 3 droplets, respectively, counted according to their fractional size.*

the nodal domain patterns of the (j,k)-modes $\varphi_{j,k}$ for $(j,k) = (1,1)$, $(2,2)$, $(2,1)$, and $(3,2)$. In each image, positive function values correspond to red, negative ones to blue, and green is for the value zero. If one of these modes is excited by noise, and if we assume that our initial mass μ is less than $-1/\sqrt{3}$, one would expect that each component of the positive nodal domain of $\varphi_{j,k}$ eventually generates one droplet, or part thereof. In fact, since the noise acts as an amplitude of the mode, these droplets should appear at the same time. For example, for $(j,k) = (1,1)$ we would expect two quarter droplets to appear in opposing corners of the domain, while for $(j,k) = (3,2)$ there should be one full interior droplet, three half droplets along the three right edges, and two quarter droplets in the two corners of the left edge. For forcing with the (j,k)-mode for $j,k \in \mathbb{N}$, one can easily see that if we count partial droplets as the corresponding fractions, then exactly $jk/2$ droplets should be generated in the domain $\Omega = (0,1)^2$. Furthermore, the resulting nucleation pattern should have exactly one possibly partial droplet in each of the components of the positive nodal domain of $\varphi_{j,k}$.

Our first set of simulation results for single mode forcing can be found in Figure 6. As in the previous section, solutions of (1.4) originate at the homogeneous state $\mu = -0.59$, and each image shows the resulting solution at time $t = 0.02547784$. While the interaction length is again chosen as $\varepsilon = 0.005$, the intensity of the noise is increased to $\sigma = 5$, since there is only a single forcing mode. In all of these simulations, the initial nucleation pattern is exactly the one determined by the positive nodal domain of the corresponding eigenmode. In the first three images, this pattern does persist up to the time of the image, and coarsening sets in at later times. In contrast, in the remaining five cases shown in Figure 6, coarsening has already begun. One can see that the observed nucleation patterns of the snapshots either exhibit small defects, such as in the top right image, or have already coarsened to a longer length scale. In the latter situations, the patterns are no longer periodic over the whole domain Ω.

For the simulations in Figure 6 the forcing modes $\varphi_{j,k}$ have comparable values for j and k. What happens if these numbers are significantly different in size, i.e., if the forcing modes are very asymmetric? For the cases $(j,k) = (5,20)$ and $(j,k) = (10,20)$ this can be seen in Figure 7, using the same parameter values and snapshot time as in the previous simulations. In both cases, the initial nucleation pattern is exactly the one determined by the positive nodal domain of the corresponding eigenmodes, and these are shown in the first and third images, respectively. This initial pattern quickly coarsens for the mode $\varphi_{20,5}$, where

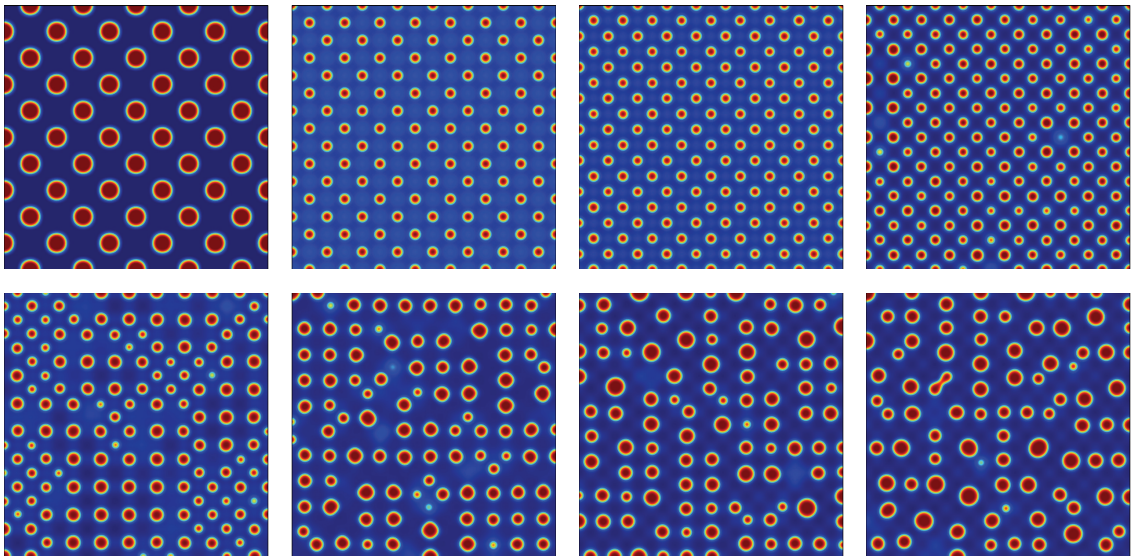

Figure 6. *Simulations for the Cahn–Hilliard–Cook equation with single mode forcing, and with interaction length* $\varepsilon = 0.005$ *and mass* $\mu = -0.59$. *Now, only the* (j,k)*-mode is forced by noise, using noise intensity* $\sigma = 5.0$. *From left to right, the images correspond to* $(j,k) = (10,10)$, $(15,15)$, $(18,17)$, $(19,18)$, $(19,19)$, $(21,21)$, $(22,22)$, *and* $(23,22)$, *respectively, and all solution snapshots are taken at the same time* $t = 0.02547784$. *In all eight cases, the initial nucleation pattern is exactly the one determined by the positive nodal domain of the corresponding eigenmode. While in the first three images this pattern persists up to the time of the image, in the remaining cases coarsening has already begun, and the nucleation pattern either exhibits defects or has already coarsened to a longer length scale.*

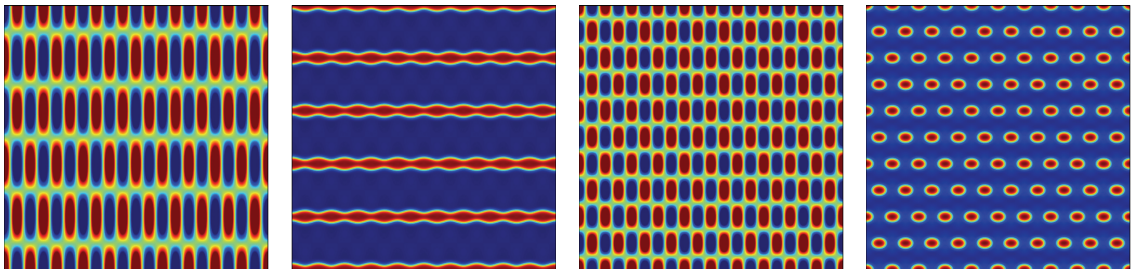

Figure 7. *Simulations for the Cahn–Hilliard–Cook equation with single mode forcing for both the* $(20,5)$*- and the* $(20,10)$*-modes, for the same parameter values as in Figure 6, including the snapshot time. The first two images show the nodal domains for the mode* $\varphi_{20,5}$, *as well as the simulation snapshot, respectively. In this case, the initial nucleation pattern is exactly the one determined by the positive nodal domain of the eigenmode, but the droplets appear round, are closely spaced in the* x*-direction, and are far apart in the* y*-direction. At the time of the snapshot, coarsening has set in and the droplets have merged to form long horizontal bands. The last two images show the nodal domains for the mode* $\varphi_{20,10}$, *as well as the simulation snapshot, respectively. In this case, the droplets persist up to the snapshot time, but their shape fluctuates due to the noise.*

the strong asymmetry leads to an unusual nucleation pattern involving elongated structures, which are clearly generated through merging of the initial droplets along horizontal lines. For the less asymmetric case shown in the right image, the nucleation pattern persists through the snapshot time, but the shape of the droplets changes with the noise to form slightly

asymmetric forms.

The simulations described in the previous two paragraphs indicate that the case of single mode forcing exhibits features similar to those of the band-limited case discussed earlier, but with a slight twist. In the single mode case, the components of the positive nodal domain of the forcing mode act as seed cells for the nucleation pattern, and for reasonably small values of the wave number $|(j,k)|$ one in fact observes very regular and periodic patterns whose droplet count increases with the wave number. We have also performed single mode simulations for considerably larger wave numbers than those shown in Figures 6 and 7. In these cases, it is no longer possible to create a nucleation pattern which supports one droplet in each component of a nodal domain of the forcing mode. Nevertheless, on a much larger time frame, nucleation can often still be observed, but with significantly fewer droplets than the predicted $jk/2$. This effect is similar to our observations in Figure 4 and will be explained in section 3.3 below.

Before closing this section, we would like to caution the reader that the single mode simulations are not necessarily a good indication of what kind of nucleation patterns can be observed if the noise acts on a small number of modes with similar wave numbers. Consider, for example, modes whose wave number deviates only slightly from a given number r; i.e., consider wave vectors (j,k) from an extremely small neighborhood of the circle of radius r in the first quadrant. For example, the (j,j)-mode corresponds to the ring with $r=\sqrt{2}j$, and forcing this mode should lead to $j^2/2$ droplets. In other words, for this mode, the number of generated droplets is proportional to r^2. In contrast, the $(k,0)$-mode lies in the ring with radius $r=k$, and it is expected to produce $k/2$ elongated structures, i.e., the nucleation pattern consists of a pattern whose number of components is proportional to r. If all the modes in an entire ring of small thickness are forced by noise, one obtains a random combination of these modes, and it is not in general the case that the superposition of modes gives rise to a function with similar number of components of the positive nodal domain. To the best of our knowledge, it is still an open question to give statistical properties on the number of components of the nodal domains for random superpositions of a certain subset of the cosine functions in the plane. Nevertheless, we do expect that such a random superposition produces droplet patterns of a characteristic width with quadratic growth of the number of droplets with respect to r. In other words, we expect that the simulations for midrange values of r reflect in some sense the patterns inherent from the frequencies of the modes. Note, however, that this heuristic based on the radius r does not explain the dropoff in droplet counts which has been observed in all of our simulations as r becomes large. Explaining this is the subject of section 3. The following observation is a summary of the findings of the section.

Observation 2.2. For small and medium frequencies, the initial geometric pattern of nucleation given by the excitation of a single spatial noise frequency can be described quite precisely as the exact regular structure given by the nodal domains of the exciting mode. After initial pattern selection, coarsening of the patterns sets in. This is particularly accentuated in the case of a mode with asymmetric nodal domains, even leading in some cases to stripe patterns. As in the band case, if the spatial frequency of the excited single mode is too high, the patterns miss forming droplets in places where the nodal domain would anticipate droplet formation. For very high spatial frequency single mode noise, no nucleation occurs in the time frame of our simulations.

2.3. Numerical simulation methods. To close this section, we briefly comment on the numerical methods which were used for the above simulations. Throughout this section, we considered the square domain $\Omega = (0,1)^2$ and homogeneous Neumann boundary conditions. Furthermore, in every case we chose the interaction length $\varepsilon = 0.005$ and total mass $\mu = -0.59$, which lies in the nucleation region. The simulations are performed using a linearly implicit pseudospectral method as described, for example, in [19]. Basically, the method is implicit in the term $-\Delta^2 u$ but explicit in the nonlinearity $-\Delta f(u)$ and in the additive noise term. Solutions are approximated using a truncated cosine series of the form

$$u(t,x,y) \approx \sum_{j,k=0}^{N-1} u_{j,k}(t)\cos(k\pi x)\cos(j\pi y) \qquad \text{with} \qquad u_{0,0}(t) \equiv \mu\ ,$$

where for the simulations of the paper we use $N = 256$. In order to avoid aliasing, the nonlinearity is computed using the two-dimensional discrete cosine transform with 512^2 discretization points. Finally, the time integration is performed using a step size $\Delta t \approx 5 \cdot 10^{-7}$. Droplet numbers are determined using thresholding of the solution data at height 0 and then applying computational homology techniques to calculate the value of Betti numbers to obtain boundary and interior droplet information. See [11, 14] for a more detailed description of these techniques.

3. Numerical continuation and pattern size. In the previous section we have developed some basic intuition for nucleation phenomena driven by different types of degenerate noise. Common to these different situations was that if the spatial frequency of the driving noise is small, much can be inferred from the nodal domain patterns of the driven eigenmodes. However, if the spatial frequency becomes too large, the nucleation patterns are usually generated at a much smaller spatial frequency. In fact, we saw in Figure 4 that this effect can be quantified, and that it manifests itself in a decrease in the droplet count. In the present section, we will explain this phenomenon through the equilibrium bifurcation structure of the deterministic Cahn–Hilliard model (1.1).

Our approach in this section is quite different from that in the last, as rather than considering direct simulations, we instead use methods of numerical bifurcation theory. This different approach allows us to see not only stable solutions, which are visible in direct simulations, but also unstable solutions, which serve as organizing centers for transient behavior. Thus, by considering this quite distinct numerical approach, we are able to gain a more complete understanding of the droplet formation seen in the direct simulations in the previous section. In particular, through this method, we will be able to deduce that for a fixed mass, there is a minimum area required for a droplet to form. Thus, if our degenerate noise forces droplets to form too close together, there will be no pattern formation at the forced length scales. Details of this result are given in Observation 3.2.

Our study will be numerical in nature, and it uses numerical continuation methods to study low energy equilibria. These solutions are found using the bifurcation and continuation software AUTO [13]. As with the direct simulations, we use a spectral Galerkin method for the continuation method, which is described in detail in [11, 21]. We begin in section 3.1 by providing some background information on stationary states of the Cahn–Hilliard equation, and by establishing some basic information on the droplet equilibria. In section 3.2 we track

the location of saddle-node bifurcation points, which in some sense provide lower bounds on the domain sizes necessary to support certain droplet configurations. This study is continued in section 3.3, where we show the surprising fact that the specific droplet configuration plays no significant role, and that any one of the saddle-node location curves can be used to find a maximal droplet carrying capacity for a given domain size. Finally, section 3.4 provides information on the typical size of the generated droplets as a function of the total mass μ.

3.1. Equilibria for the deterministic system. As a dissipative parabolic partial differential equation, the deterministic Cahn–Hilliard equation (1.1) has a compact global attractor which describes its long-term dynamics; see, for example, [33]. This attractor is comprised of equilibrium solutions as well as heteroclinic solutions between these stationary states. For practical applications, however, one generally needs more information on the actual structure of the attractor than only a statement of its existence.

For the case of one-dimensional domains such results have been obtained in the past. Grinfeld and Novick-Cohen [16] used a phase plane analysis in combination with transversality arguments to completely describe the set of equilibria of the Cahn–Hilliard model in this situation for every value of the total mass μ. Furthermore, Mischaikow [28] was able to establish the dynamics on the attractor by constructing a semiconjugacy to a finite-dimensional model, based on Conley index methods. However, the latter result is only valid for mass values in the spinodal region $-1/\sqrt{3} < \mu < 1/\sqrt{3}$, and little is known rigorously in the nucleation region. See [2] for more details.

While there are partial results on one-dimensional domains Ω, the situation is wide open in the two- and higher-dimensional cases. There are basically no rigorous results available on the complete attractor structure, even for simple domains. The observed equilibrium structure is generally elaborate and complex, and the bifurcation diagrams contain many secondary and ternary bifurcations; see, for example, Figure 8. In fact, it is our belief that finding a description of the full attractor is intractable in the higher-dimensional case. This is particularly true in the nucleation regime, as the homogeneous trivial state has no bifurcating branches. We would like to point out, however, that computer-assisted proofs can be obtained to describe part of the attractor structure. See, for example, [24] for the verification of stationary states, [25] for the existence of heteroclinics, and [37, 38] for a recent simplification of the equilibrium verification approach.

In light of the above discussion it is not surprising that we are not attempting a full understanding of the attractor structure in order to explain our nucleation observations. Instead, we focus on the equilibrium solutions which can be used to explain the nucleation failures seen in the simulation results from the previous section. For convenience of discussion, we introduce the new parameter

$$\lambda = 1/\varepsilon^2 \, .$$

Then a function $u : \Omega \to \mathbb{R}$ is an equilibrium solution of the deterministic Cahn–Hilliard

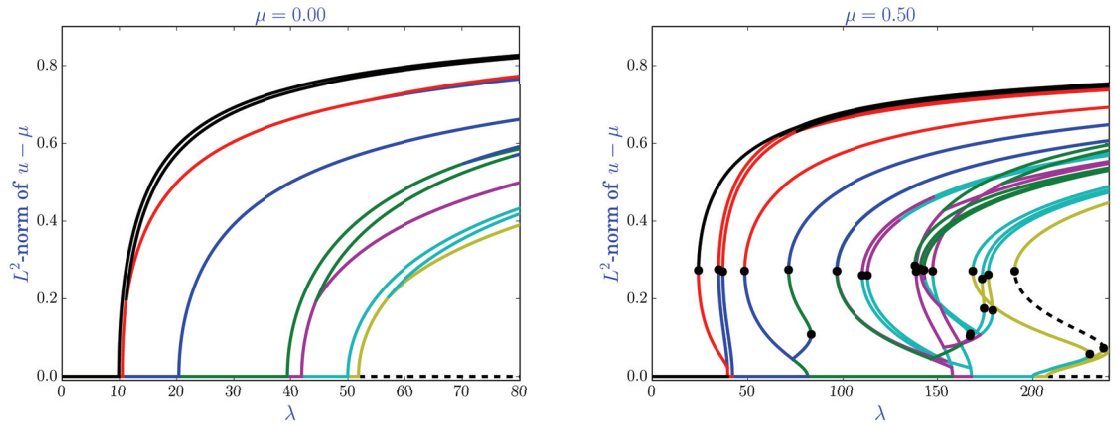

Figure 8. *Equilibrium bifurcation structure for the Cahn–Hilliard equation (1.1) on the two-dimensional domain $\Omega = (0,1) \times (0, 0.97)$. The left image is for total mass $\mu = 0$, while the right image is for $\mu = 1/2$. In both panels, the horizontal axis uses the parameter $\lambda = 1/\varepsilon^2$, and the vertical axis shows the $L^2(\Omega)$-norm of $u - \mu$, where u denotes the equilibrium and μ its total mass. The equilibria are colored based on their stability index, with black for index zero, i.e., stable solutions, and red, blue, green, magenta, cyan, yellow, and dashed black corresponding to indices $1, \dots, 7$, respectively. Black dots indicate saddle-node bifurcation points.*

model (1.1) if and only if it solves the nonlinear elliptic system

$$
\begin{aligned}
-\Delta\left(\Delta u + \lambda f(u)\right) &= 0 \quad \text{in} \quad \Omega\,, \\
\frac{\partial u}{\partial \nu} = \frac{\partial \Delta u}{\partial \nu} &= 0 \quad \text{on} \quad \partial\Omega\,, \\
\mu &= \frac{1}{|\Omega|}\int_\Omega u \, dx\,,
\end{aligned}
\tag{3.1}
$$

where we consider both λ and μ as bifurcation parameters. It was already pointed out in the introduction that there is a symmetry between negative and positive values of the total mass μ; i.e., we now restrict our attention to the case of positive mass $\mu > 0$ without loss of generality.

The stationary Cahn–Hilliard system (3.1) exhibits a scaling property which will be useful later. To state this property, assume that $u : \Omega \to \mathbb{R}$ is an equilibrium for the parameter value $\lambda = \lambda_0 = 1/\varepsilon_0^2$ and with total mass μ_0 on the square domain $\Omega = (0,1)^2$. Then for any real number $\lambda_n > 0$ the rescaled function

$$
x \mapsto u\left(\sqrt{\frac{\lambda_n}{\lambda_0}} \cdot x\right) = u\left({}^{\varepsilon_0}\!/_{\varepsilon_n}\, x\right)
$$

is a solution of (3.1) for $\lambda = \lambda_n$ and $\mu = \mu_0$ on the rescaled domain

$$
\widetilde{\Omega} = \left(0, \sqrt{{}^{\lambda_0}\!/_{\lambda_n}}\right)^2 .
$$

Reformulating these statements implies that studying the set of equilibria for

$$
(\lambda, \mu) = (\lambda_n, \mu_0) \qquad \text{on the domain} \qquad \widetilde{\Omega} = (0, L)^2
$$

is equivalent to studying the set of equilibria for

$$(\lambda, \mu) = \left(L^2 \lambda_n, \mu_0\right) \qquad \text{on the domain} \qquad \Omega = (0,1)^2 \, .$$

This scaling argument shows that changing the size of the underlying domain while keeping λ fixed can equivalently be viewed as changing the parameter λ on a fixed domain while the total mass remains unaffected by the scaling.

In our situation, we are interested in stationary solutions of the deterministic Cahn–Hilliard model with droplet structure. For the simulations shown in the last section, we usually encounter many small droplets in the domain Ω or, equivalently, many droplets of size of order one on a large domain. Rather than trying to find equilibrium solutions which contain such a large number of droplets, we take the point of view used in [11, 35] that understanding bulk effects of many droplets on a large domain can be accomplished by considering small domains which sustain either a single droplet or a small number of droplets. Applying the scaling argument again shows that this is equivalent to studying the fixed domain $\Omega = (0,1)^2$, but for relatively small values of λ, meaning that this is computationally feasible.

As mentioned earlier, our study of the equilibrium structure of (3.1) is numerical in nature. More precisely, we use path-following techniques based on AUTO [13] to track nontrivial solution branches of equilibrium solutions for varying parameter λ, as they bifurcate from the known homogeneous stationary state μ. This leads to bifurcation diagrams such as those shown in Figure 8, which were computed for the rectangular domain $\Omega = (0,1) \times (0, 0.97)$. While at first glance this choice of domain might seem strange, it is essential to simplify the path-following process. On the unit square, most of the bifurcation points from the trivial homogeneous equilibrium have at least a two-dimensional bifurcation kernel, which makes resolving all (usually) multiple bifurcating branches difficult. We therefore slightly perturb the domain in the above way to break up these higher-dimensional bifurcation points into simple ones. This small domain perturbation will be removed later; see our discussion at the end of this section.

For total mass $\mu = 0$ and $0 < \lambda \leq 80$ one obtains the bifurcation diagram shown on the left in Figure 8. The horizontal line at the bottom of the figure corresponds to the homogeneous equilibrium, and a number of branches are bifurcating from this trivial solution. The fact that we plot the $L^2(\Omega)$-norm of u in the vertical direction, combined with the symmetries in the equation, implies that each point on the shown nontrivial solution branches corresponds to at least two nontrivial equilibria, and sometimes to more than two. The branches are colored based on the stability index of the stationary states, with black corresponding to index zero, i.e., stable solutions, and red, blue, green, magenta, cyan, yellow, and dashed black corresponding to indices $1, \ldots, 7$, respectively. Notice that the Cahn–Hilliard equation on this two-dimensional domain contains multiple stable states, and that the bifurcation diagram is fairly elaborate. In contrast, the right panel in Figure 8 shows the bifurcation structure of (3.1) for $\mu = 1/2$ and $0 < \lambda \leq 240$, and we now plot the $L^2(\Omega)$-norm of $u - \mu$ in the vertical direction. Note that the bifurcation points from the trivial solution now occur at larger λ-values than in the case $\mu = 0$, and that many of the bifurcations turn from super- to subcritical. In this way, a number of saddle-node bifurcations are formed in the bifurcation diagram. These saddle-node bifurcations are crucial to our discussion.

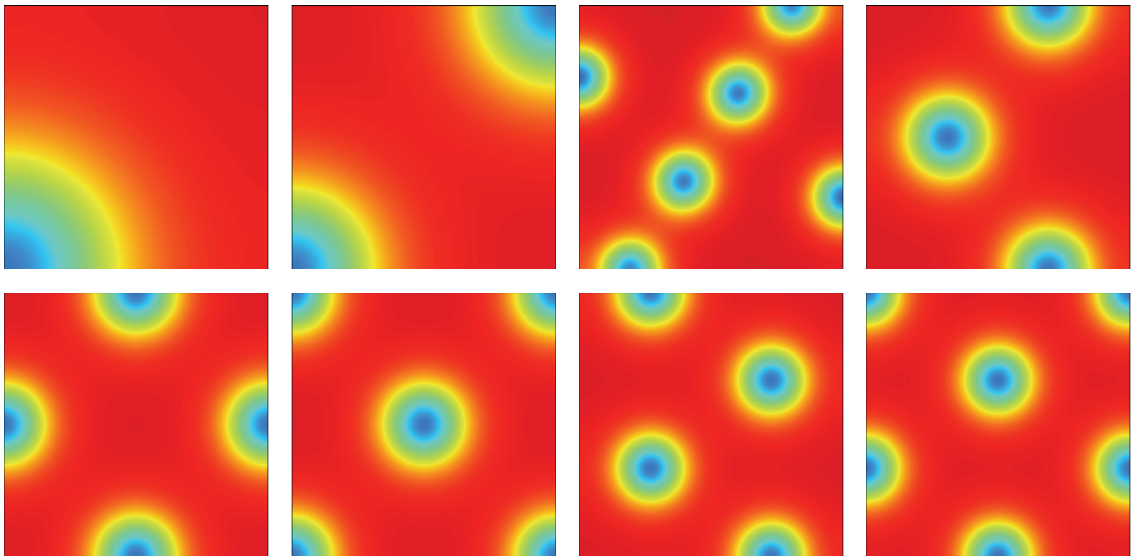

Figure 9. *Droplet equilibria for the Cahn–Hilliard equation for total mass $\mu = 0.6$ on the domain $\Omega = (0,1)^2$. These solutions occur at distinct λ-values and are obtained by following solutions on the nontrivial branches in the right image of Figure 8 with respect to increasing μ. From top left to bottom right, we label the above solutions as* 10, 11, 13, 21, 22a, 22b, 31, *and* 32, *consistent with the branch numbering scheme used in Figure 11 below.*

We would like to point out that both mass values $\mu = 0$ and $\mu = 1/2$ are contained in the spinodal region since $1/\sqrt{3} \approx 0.57735$. One can show that as we increase the mass μ toward $1/\sqrt{3}$, all bifurcation points from the trivial solution line will converge toward positive infinity, such that for mass values $\mu > 1/\sqrt{3}$, there are no more bifurcations from the trivial homogeneous solution line. This is to be expected, since in the nucleation region the homogeneous state is stable for all values of the parameter $\lambda = 1/\varepsilon^2$. In other words, since we are interested in solutions of (3.1) for mass values in the nucleation region, we cannot simply use path-following from the trivial solution in this setting. Instead, we follow the solutions along the nontrivial branches found at $\mu = 1/2$ as we increase the mass parameter μ into the nucleation regime. In this way, we can find nontrivial equilibrium solutions for the Cahn–Hilliard equation in the nucleation regime which consist of a small number of droplets. Furthermore, since we will be interested in scaling results later, it will be useful to have these equilibrium solutions again on the unit square $(0,1)^2$. This can be achieved by considering the parameter-dependent domains $\Omega_a = (0,1) \times (0,a)$ and continuing the solutions from Figure 8 for fixed mass $\mu = 1/2$ from $a = 0.97$ to $a = 1$. Note that this is possible, as the symmetry issues that led us to consider a rectangular domain are no longer a problem, since at this step we are considering solutions far from the homogeneous equilibrium.

The results of this sequence of three continuation computations can be found in Figure 9, which shows a variety of equilibrium solutions of the deterministic Cahn–Hilliard model on the domain $\Omega = (0,1)^2$, and for mass $\mu = 0.6$. Note that the depicted solutions occur at distinct λ-values. From top left to bottom right, we label the solutions in the figure as 10, 11, 13, 21, 22a, 22b, 31, and 32, consistent with the branch numbering scheme used in Figure 11.

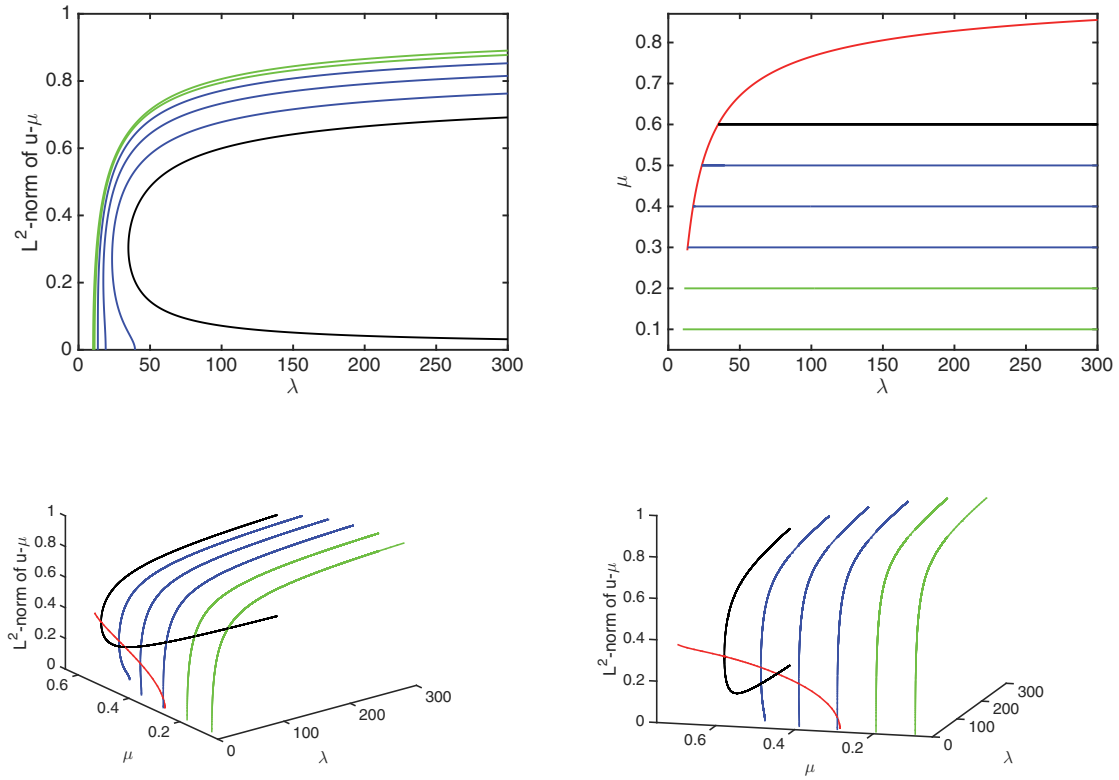

Figure 10. *Bifurcation diagrams for the quarter droplet shown in the first image of Figure 9. In the top left image, we show the bifurcation curves corresponding to the quarter droplet for different μ-values. The case $\mu = 0.6$ leads to the black curve, which is not connected to the trivial solution line. Moving toward the left from its saddle-node bifurcation point, the curves are for $\mu = 0.5, 0.4, \ldots, 0.1$. Note that for $\mu = 0.1, 0.2$ (green) the curves bifurcate in a pitchfork bifurcation from the homogeneous equilibrium, are strictly increasing, and have no secondary bifurcations. In contrast, for $\mu = 0.3, 0.4, 0.5$ (blue) the curves arise from the homogeneous state via a subcritical pitchfork bifurcation before reversing direction in a saddle-node point. Only the black curve, with $\mu = 0.6$, is contained in the nucleation region. The top right image shows these six bifurcation curves projected down onto the λ-μ-parameter plane. Moreover, the red curve in the image shows the location of the saddle-node bifurcation points, computed also for intermediate μ-values. Finally, the two images in the bottom row depict all this information in all three dimensions, shown from two different angles.*

In particular, a label starting with jk indicates that the solution was found via a nontrivial branch in Figure 8 arising through a bifurcation kernel at the trivial solution spanned by the mode $\varphi_{j,k}$ introduced in the previous section.

3.2. Location curves of saddle-node bifurcations. After the preparations of section 3.1 we can now tackle the droplet carrying capacity of a domain. This will be accomplished by studying the bifurcation branches of the droplet equilibria shown in Figure 9.

As a first step, we consider the quarter droplet equilibrium shown in the top left image of Figure 9 for $\mu = 0.6$. If we keep the mass fixed and consider λ as a free parameter, this solution lies on a smooth curve of equilibrium solutions of (3.1). The resulting solution branch is shown in black in the top left image of Figure 10. Notice that as λ increases from zero,

this branch is created via a saddle-node bifurcation at around $\lambda \approx 34.827$, and its two halves continue as smooth curves with increasing λ. As a second step, consider the black branch, but slowly decrease the mass μ. Then this branch can be continued to a nearby curve of solutions, and for $\mu = 0.5, 0.4, \ldots, 0.1$ the resulting curve continuations are shown in the top left image of Figure 10, from right to left. As μ decreases from $\mu = 0.6$, these curves initially all originate in a saddle-node bifurcation. This is true for the cases $\mu = 0.5, 0.4, 0.3$, which are shown in blue. Between $\mu = 0.3$ and $\mu = 0.2$, the curves lose their saddle-node bifurcation and originate via a pitchfork bifurcation from the trivial homogeneous state. This is the case for $\mu = 0.2$ and 0.1 shown in green. The top right image of Figure 10 shows these six solution curves again, but projected down onto the λ-μ-parameter plane. In addition, the red curve represents the location of the saddle-node bifurcation points for all curves originating in such a way. Finally, the two images in the bottom row depict all this information in three dimensions, shown from two different angles.

It is natural to wonder what the curves in Figure 10 have to do with the droplet carrying capacity mentioned earlier. To see this, we take another look at the red curve shown in the upper right image of the figure. Let (λ^*, μ^*) be a point on this curve. Then for fixed mass $\mu = \mu^*$, equilibrium solutions in the form of a quarter droplet only exist for $\lambda \geq \lambda^*$. In view of our scaling discussion at the end of section 3.1, and since we keep our underlying domain Ω fixed, we can therefore view λ^* as a measure for the smallest domain size on which a quarter droplet can be supported. For example, we have already seen that for $\mu^* = 0.6$ one obtains $\lambda^* \approx 34.827$.

While the above reasoning does provide a lower bound, this bound is clearly dependent on the quarter droplet configuration. However, Figure 9 shows that there are many other equilibria which contain droplets, and they too should give rise to lower bounds. This is demonstrated in Figure 11. For each of the remaining seven equilibria of Figure 9 we computed their associated bifurcation branches with λ as bifurcation parameter, and again we find that for certain mass values these branches originate in a saddle-node bifurcation. Collecting all locations of saddle-node bifurcation points then furnishes the left image of Figure 11. Each curve in this image corresponds to the location of saddle-node bifurcation points, labeled according to the equilibria in Figure 9, and computed via two-parameter continuation. For example, the curve labeled 10 is the same location curve as that shown in Figure 10 in red, and the curve labeled 11 is for the equilibrium solution with two quarter droplets in opposite corners of the domain. Both of these curves were only computed up to $\lambda = 300$, even though they do continue for larger λ-values as well. As expected, for each of the new equilibrium solutions we obtain lower domain size bounds which are larger than the quarter droplet bound contained above. Furthermore, for some equilibrium solutions the saddle-node location curves consist of two parts merging in a cusp. This is due to the fact that on some equilibrium bifurcation curves there are two saddle-node bifurcation points. This can be seen in the right image in Figure 8, where the fifth saddle-node bifurcation from the left lies on a branch with a second fold.

3.3. Estimation of sustained pattern size. At first glance the saddle-node location curves in the left image of Figure 11 seem overwhelming; for every droplet configuration and every value of $\mu = \mu^*$ there are many lower bounds λ^* on the domain's size, depending on the

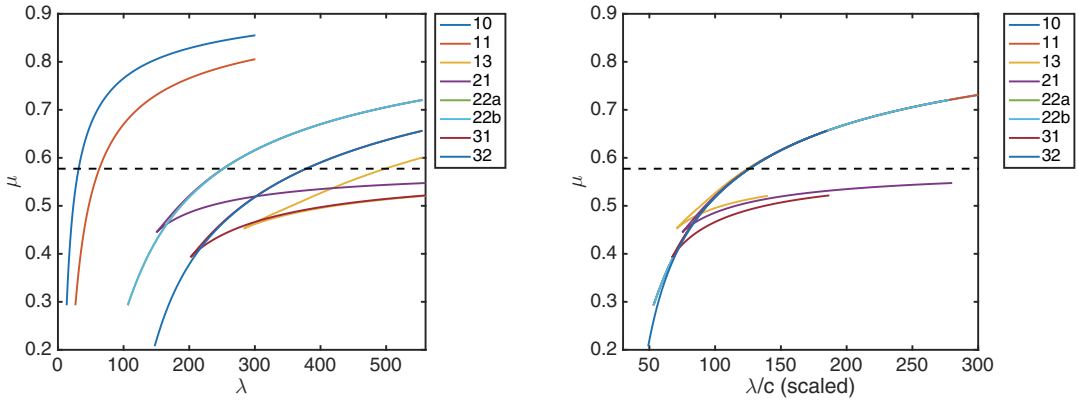

Figure 11. *Location curves for saddle-node bifurcation points. The left image shows the location of saddle-node bifurcation points on the solution branches which correspond to the eight equilibria in Figure 9. The blue curve labeled* 10 *is the same location curve as that shown in Figure 10 in red, while the remaining curves are for the other seven droplet equilibria. In the right image, the same curves are shown, but now the* λ*-values in each curve are scaled by the (possibly fractional) droplet count* c *of the associated equilibrium. In both images, the dashed black line indicates the boundary between the spinodal regime (below) and the nucleation region (above). Note that the curves labeled* 10 *and* 11 *in the left image are only partially computed. They do in fact continue to the right for all values of* λ*.*

specific equilibrium. Note, however, that in this image there appear to be only five curves in the nucleation regime for the eight types of equilibria. In fact, there are eight curves, but those for equilibria with labels 21, 22a, and 22b overlap exactly, as do the two curves for labels 31 and 32. For a heuristic understanding of this, we appeal to the system energy (1.2). Consider the contribution to the energy provided by an equilibrium containing boundary droplets, interior droplets, or corner droplets, where μ and λ are fixed. Make the simplifying assumption that the solution is essentially constant $+1$ inside the droplet and constant -1 outside the droplet, where those constants correspond to the zeros of F in (1.2). In this case, the only contribution to the energy $E_\varepsilon[u]$ occurs in the transition layer between the interior and exterior of the droplet, when the energy depends almost entirely on $\varepsilon^2 = 1/\lambda$ times the integral of the gradient. If the three types of solutions have the same radius, then the interior droplet has twice the circumference of the boundary droplet and four times the circumference of the corner droplet. Therefore, we expect that if one interior droplet solution occurs at (μ, λ), then the one boundary droplet solution would be sustained at the same energy for parameters $(\mu, \lambda/2)$, and the one corner droplet solution will occur at $(\mu, \lambda/4)$. More generally, for an equilibrium with any number of droplets, let c be the possibly fractional number of droplets within the equilibrium solution. Then equilibria with the same value of c should occur at almost the same parameter values. For the equilibria in Figure 9, we obtain counts $c = 1/4$, $1/2$, 4, 2, 2, 2, 3, and 3, respectively, from top left to bottom right; and the saddle-node location curves for equilibria with the same droplet count c overlap exactly in the nucleation region.

In fact, even more is true. Consider again a point (λ^*, μ^*) on the saddle-node location curve for the quarter droplet. Since λ^* is a measure for the smallest domain size supporting

a quarter droplet, $4\lambda^*$ should be a measure for the smallest domain size supporting a full droplet. In other words, in order to get domain sizes for single droplets, one should be scaling the λ-value of the location curves in the left image of Figure 11 by the associated droplet count c. The resulting scaled curves are shown in the right image of Figure 11, and they coincide in the nucleation region! In other words, regardless of the actual droplet structure in the considered equilibrium, one obtains a universal curve which describes the minimal domain size necessary for supporting a droplet as a function of the total mass μ. This leads to the following definition.

Definition 3.1 (droplet capacity function). *For the deterministic Cahn–Hilliard equation* (1.1) *on the unit square* $\Omega = (0,1)^2$*, we define the* droplet capacity function $\lambda = \Lambda(\mu)$ *in the following way. For every mass* $1/\sqrt{3} < \mu < 1$ *in the nucleation region the value* $\Lambda(\mu) > 0$ *denotes the* λ*-coordinate of the saddle-node bifurcation point on the quarter droplet solution branch multiplied by four.*

Based on our above discussion, the droplet capacity function numerically coincides with all of the rescaled curves shown in the right image of Figure 11. Furthermore, by using a standard least-squares fitting approach we obtain that for μ-values in the nucleation regime we get the approximation

$$\Lambda(\mu) \;\approx\; \frac{24.08392}{(1-\mu)^{1.912156}} \qquad \text{for} \qquad \frac{1}{\sqrt{3}} < \mu < 1\,. \tag{3.2}$$

In other words, we would expect a proportionality of the form $\Lambda(\mu) \sim (1-\mu)^{-2}$ as $\mu \to 1$. This will be discussed in more detail in section 3.4.

We can now try to use the droplet capacity function to estimate the maximal number of droplets which can be supported in a given domain and for given values of ε and μ in (1.1). In view of the rescaling arguments from the end of section 3.1, we restrict our attention to the specific domain $\Omega = (0,1)^2$ and consider only ε and μ as variable. Domains Ω of size different from one can then be treated via rescaling. Then we conjecture that the following holds:

(C) *If the total mass* μ *is fixed in the nucleation region and if* $\varepsilon > 0$*, then a nucleation simulation of the stochastic Cahn–Hilliard–Cook model* (1.4) *on the domain* $\Omega = (0,1)^2$

$$\textit{can support at most} \quad \frac{\lambda}{\Lambda(\mu)} = \frac{1}{\varepsilon^2 \Lambda(\mu)} \quad \textit{droplets}\,, \tag{3.3}$$

where $\lambda = 1/\varepsilon^2$ *and* $\Lambda(\mu)$ *denotes the droplet capacity function from Definition 3.1.*

The above formula follows directly from the scaling arguments at the end of section 3.1, by assuming that a domain of a given size can be equipartitioned into smaller domains, each of which is of the minimal size necessary to support exactly one droplet.

How does the formula in (3.3) relate to our earlier simulations? For the types of degenerate noise considered in this paper, we are forcing modes on a more or less regular grid with a nearly fixed wavelength. The forcing wavelength is then expected to determine the single-droplet domains. For example, consider the single mode degenerate noise case. Forcing the mode $\varphi_{j,k}$ excites a pattern with $jk/2$ droplets. At $\mu = -0.59$ and $\varepsilon = 0.005$ our conjecture (C) implies that the Cahn–Hilliard–Cook model can support at most

$$\frac{\lambda}{\Lambda(\mu)} \;\approx\; 200^2 \cdot \frac{(1-|\mu|)^{1.912156}}{24.08392} \;\approx\; 301.9362$$

droplets. For the (j,k)-mode this leads to the restriction

$$\frac{jk}{2} \leq 301.9362 \qquad \Longleftrightarrow \qquad jk \leq 603.8724\ .$$

Notice that for all values of (j,k) used in Figures 6 and 7, the product jk satisfies the last inequality, and indeed we see the initial nucleation patterns in the form of the components of the positive nodal domains. Furthermore, our additional simulations show that even if jk is only slightly larger than 603, nucleation in the pattern determined by the mode does not seem to be possible.

If instead of the (j,k)-mode we force the symmetric (k,k)-mode, then according to the above formula the maximum value k for which degenerate forcing of $\varphi_{k,k}$ can be expected to create a sustained nucleation droplet pattern which is determined by the nodal domains is given by $k_{max} = 24 = \lfloor 24.5738 \rfloor = \lfloor \sqrt{603.8724} \rfloor$. This is in amazing agreement with the results of Figure 4.

We can now return to the band-limited noise simulations from the last section. We have seen that for large radii r_0 there seem to be no nucleation events in the interior domain, and only very few nuclei at the boundary of the domain, if at all. Our above discussion seems to indicate that this is due to the fact that in the interior of the domain, the wave number of seed cells is too large to allow for sustained nucleation events. We summarize this in the following observation.

Observation 3.2. For band-limited noise, there is a radius $R_0 = 2/(\sqrt{\lambda_0}\varepsilon)$ such that the pattern size of the noisy perturbation is too small to ignite spontaneous nucleation for lower band radii $r_0 > R_0$, even if the noise strength is sufficiently large and the solution is of order $\mathcal{O}(1)$.

3.4. Scaling of droplet size. In the last section we have shown that the droplet capacity function Λ introduced in Definition 3.1 can be used to determine the maximal number of droplets which can be supported by the Cahn–Hilliard–Cook equation at the beginning of the nucleation process. In fact, we have seen in (3.2) that for mass values μ in the nucleation region the proportionality $\Lambda(\mu) \sim (1-\mu)^{-2}$ seems to be satisfied. We now briefly relate this scaling to the actual observed size of the individual droplets.

We have already seen at the beginning of section 3.3 that it can be useful to think of the droplet equilibrium solutions as being almost equal to a step function with values ± 1. In reality, of course, this is not the case. In fact, as the examples in Figure 12 show, the equilibria at the saddle-node bifurcation points of Figure 11 are usually far from the idealized piecewise constant situation; their function values do not even have to be close to ± 1. Nevertheless, the droplets contained in the saddle-node equilibria are of circular form, and one can therefore easily determine their radius from the numerical path-following data. This can be accomplished in two ways. On the one hand, one can threshold the equilibrium solutions at the level $u = 0$ and determine a first radius estimate r_1 by measuring the maximal droplet size in the x-direction directly. On the other hand, one can find the area A of each of the possibly fractional droplets. Then one obtains a second estimate r_2 for the radius via the formula $\sqrt{qA/\pi}$, where $q \in \{1/4, 1/2, 1\}$ denotes the appropriate droplet fraction contained in the equilibrium.

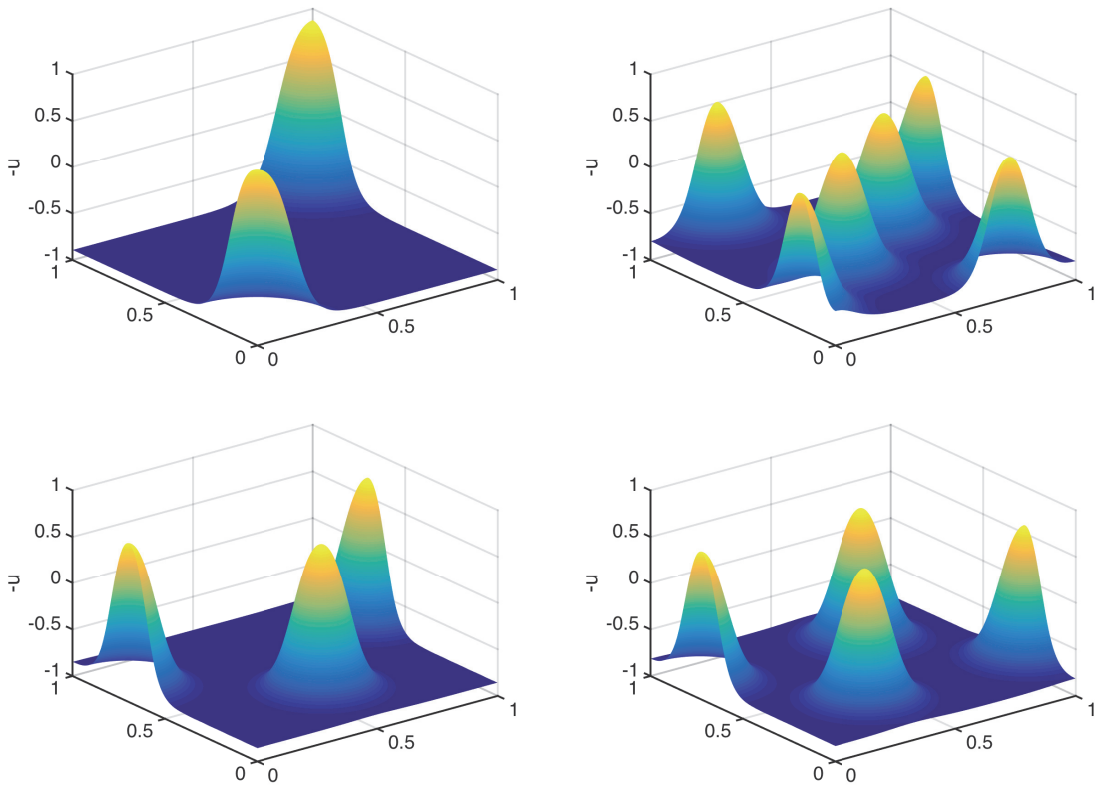

Figure 12. *Geometry of the equilibrium solutions of* (3.1) *at the saddle-node bifurcation points. From top left to bottom right, the images show solutions on the branches labeled* 11, 13, 21, *and* 31, *respectively, in the nucleation region of Figure* 11. *The top left image is for* $\lambda = 300$, *and the remaining images are for* $\lambda = 550$. *Since the mass values* μ *are all positive, the images show* $-u$ *rather than* u.

For the case of the quarter droplet branch labeled 10 in Figure 9 the resulting radii r_1 and r_2 are shown in the left image of Figure 13. We would like to point out that similar computations for the droplets in the remaining saddle-node equilibria lead to identical curves, after the domains have been rescaled by the total equilibrium droplet count c. In this sense, the droplet radius as determined by the droplet capacity function $\Lambda(\mu)$ is determined uniquely by the mass μ.

As it turns out, we can say even more. For this we return to the sharp interface limit, despite the fact that the saddle-node equilibria generally do not exhibit sharp interfaces. Assume that the function $u : (0,1) \to \{\pm 1\}$ has a negative quarter droplet in one corner of the domain and is equal to $+1$ everywhere else. If we also assume that the total mass of the function u equals $\mu > 0$, then the radius r_μ of the quarter droplet has to satisfy the identity

$$\mu \;=\; -\frac{\pi r_\mu^2}{4} + \left(1 - \frac{\pi r_\mu^2}{4}\right) \;=\; 1 - \frac{\pi r_\mu^2}{2}\,; \qquad \text{i.e., we have} \qquad r_\mu \;=\; \sqrt{\frac{2(1-\mu)}{\pi}}\,.$$

This sharp interface limit radius r_μ is shown in the left image of Figure 13 as a solid red line, which seems to indicate that as μ increases toward 1 this radius decreases proportionally

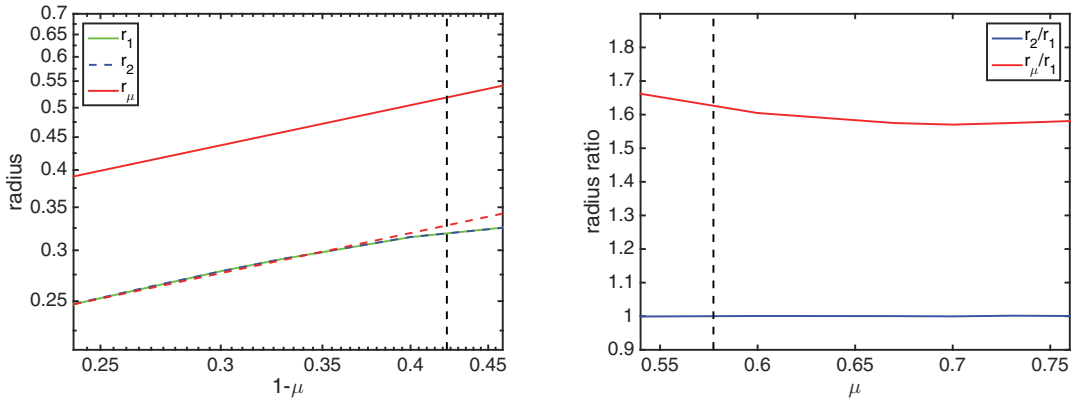

Figure 13. *Size of the droplets in the saddle-node equilibrium solutions leading to Figure 11. The left image shows the radius estimates r_1 and r_2 described in the text for the quarter droplet solution labeled 10 in green and dashed blue, respectively. In addition, we also show the radius r_μ determined from the sharp interface limit in red, and the scaled curve $0.6323\, r_\mu$ in dashed red. The right image depicts the ratios r_2/r_1 and r_μ/r_1 as a function of μ. While the above images are only for the quarter droplet, they remain valid for the remaining equilibria in Figure 9 after suitable rescaling by the total equilibrium droplet count c.*

to both of our numerical estimates r_1 and r_2. See also the right image of the figure, which plots the ratios r_2/r_1 and r_μ/r_1 as a function of μ. Thus, it seems that in the limit $\mu \to 1$ the droplet radius is in fact predicted by the sharp interface limit, despite the equilibrium geometries observed in Figure 12.

Observation 3.3. The saddle-node bifurcation points give a good prediction for the total number of droplets possible at a given ε-value for a mass in the nucleation region. Although the equilibrium solutions at the saddle-node bifurcation points do not have sharp interfaces, when the total mass of one component significantly dominates the total mass of the other component, the size of the droplets is proportional to the size expected by assuming sharp interface limits, meaning that there is no transition layer between the two components. We have given a precise formula for the droplet size in this sharp interface limit.

4. Analytic estimates for the nucleation time frame.

In this section, we present analytic bounds which address the nucleation time frame in the degenerate noise setting. The goal of this section is to give a rigorous proof of our numerical observations from the previous two sections in the asymptotic regime for $\varepsilon \to 0$. Our main result is sketched in the following observation, with the precise rigorous estimates filled in as we develop the theoretical results throughout this section. We focus first on the linearized equation and give a brief sketch of how the linear arguments can be carried over to the nonlinear setting of (1.4) at the end of this section.

Observation 4.1 (solution size for the linearized problem). Consider a solution to the linearized stochastic Cahn–Hilliard equation, which is given in detail below in (4.2). Then the following holds for two constants S_0 and S_δ relating the linear damping and the noise strength such that $S_0 < S_\delta$. These constants are defined later in Assumption 4.4.

- For noise strengths σ much smaller than $1/S_\delta$, the solutions of the linearized Cahn–Hilliard–Cook model in the nucleation regime stay small over very large time intervals,

which are almost of exponential size.

- For noise strengths σ much larger than $1/S_0$, and after relatively short times of order $\max\{1/|\eta_k| \,:\, k \in I\}$, the solutions of the linearized Cahn–Hilliard–Cook model become large with high probability. The numbers η_k in this formulation denote the dominant eigenvalues of the linearized Cahn–Hilliard equation, where the eigenvalues were defined in (1.3) and the index set for the dominant eigenvalues is given in (4.1).

That is, for sufficiently small noise strengths, we are very unlikely to ever see nucleation, whereas for sufficiently large noise strengths, we are very likely to see nucleation.

In order to fix ideas for considering how the theoretical methods in this section apply to the numerical results in the previous sections, we state exactly what our theory shows for the following example, leaving the details of the proof for the later parts of the section.

Example 4.2. Consider the case of band-limited noise in two space dimensions as in section 2 on the domain $\Omega = (0,1)^2$. In this case, for two radii $0 < r_0 < r_1 = r_0 + d$, where we consider d fixed and vary r_0, we used the index set

$$I = \left\{ k \in \mathbb{N}^2 \,:\, r_0 < |k| < r_1 \right\} . \tag{4.1}$$

Moreover, based on the eigenvalue formula given in (1.3), and due to the fact that $f'(\mu) < 0$ in the nucleation region, one obtains for all $k \in I$ the inequalities

$$-\pi^2 r_1^2 \left(\varepsilon^2 \pi^2 r_1^2 - f'(\mu)\right) \;<\; \eta_k \;<\; -\pi^2 r_0^2 \left(\varepsilon^2 \pi^2 r_0^2 - f'(\mu)\right) .$$

Thus, the size of the eigenvalues η_k satisfies

$$\eta_k \;\sim\; \begin{cases} -r_0^2 & \text{for} \quad 1 < r_0 < 1/\varepsilon \,, \\ -\varepsilon^2 r_0^4 & \text{for} \quad r_0 > 1/\varepsilon \,. \end{cases}$$

Moreover, the number of elements in the index set I is proportional to the area of the quarter ring; i.e., we have $|I| = \pi(r_1^2 - r_0^2)/4 = \pi d(2r_0 + d)/4 \sim r_0$ for $r_0 > 1$, since we keep the ring width d fixed. We will see later that this implies for all small $\delta > 0$ the following bound for the constant S_δ from the previous observation:

$$S_\delta \;\sim\; \begin{cases} r_0^{-1+2\delta} & \text{for} \quad 1 < r_0 < 1/\varepsilon \,, \\ \varepsilon^{-2+2\delta}\, r_0^{-3+4\delta} & \text{for} \quad r_0 > 1/\varepsilon \,. \end{cases}$$

If we fix the noise strength as $\sigma = \varepsilon^\tau$ and let $r_0 = \varepsilon^{-\varrho}$ with $\tau \geq 0$ and $\varrho \geq 0$, then we can observe the following two scenarios for all sufficiently small $0 < \varepsilon \ll 1$.

- If $0 \leq \varrho < 1$, then $r_0 = \varepsilon^{-\varrho} \ll \varepsilon^{-1}$; i.e., we have $\sigma^2 S_\delta \sim \varepsilon^{2\tau + \varrho(1-2\delta)}$. This implies that with high probability there is no spontaneous nucleation on any time scale which is a positive power in $1/\varepsilon$, as long as we have $2\tau + \varrho(1-2\delta) > 0$. By the below-given Assumption 4.4 we have $\delta < 1/2$, and therefore this is satisfied if either τ or ϱ is strictly positive.
- Alternatively, if $\varrho > 1$, then $r_0 = \varepsilon^{-\varrho} \gg \varepsilon^{-1}$; i.e., we have $\sigma^2 S_\delta \sim \varepsilon^{2\tau + 3\varrho - 2 + \delta(2-4\varrho)}$. Thus, with high probability there is no spontaneous nucleation on any time scale which

is a positive power in $1/\varepsilon$, as long as we have $2\tau + \varrho(3-4\delta) - 2 + 2\delta > 0$, and since by Assumption 4.4 (to be stated formally below) we have $\delta < 1/2$, this condition holds as long as $2\tau + \varrho > 2$. In fact, if we assume further that $\delta < 1/4$, then this condition holds for every $\varrho > 1$.

In other words, as long as the radius r_0 grows unboundedly as $\varepsilon \to 0$, we do not expect to see nucleation on time intervals whose length is polynomial in $1/\varepsilon$. If, on the other hand, the radius is of order one, then we need the noise intensity to decay toward zero with ε in order for the same statement to hold.

Since we are mostly interested in the initial nucleation regime, rather than considering the nonlinear equation (1.4), we restrict our attention to the linearized equation at the homogeneous state μ, which is given by

$$\begin{aligned} v_t &= -\Delta(\varepsilon^2 \Delta v + f'(\mu)v) + \sigma \cdot \xi \quad \text{in} \quad \Omega\,, \\ &\qquad \frac{\partial v}{\partial \nu} = \frac{\partial \Delta v}{\partial \nu} = 0 \quad \text{on} \quad \partial\Omega \end{aligned} \tag{4.2}$$

and subject to the mass constraint $\int_\Omega v\,dx = 0$. More precisely, we derive estimates for the stochastic convolution, which is the solution of (4.2) originating at the zero initial condition. This can be carried over to the nonlinear case, and we comment on that later. In addition, we focus on the asymptotic regime of small interaction length $0 < \varepsilon \ll 1$.

The remainder of the section is organized as follows. In section 4.1 we derive an upper bound on the stochastic convolution, which can be used to rule out the formation of nucleation droplets over large time intervals, at least in the asymptotic regime. It provides a lower bound on the nucleation time scale, which is extremely large. After that, section 4.2 is devoted to establishing a lower bound for the maximum norm of the stochastic convolution, which indicates that nucleation events are likely to be triggered. We point out here that both bounds will lead to time frames which have similar orders of magnitude. At the end of the section, we briefly indicate how these results can be carried over to the nonlinear problem (1.4).

4.1. Upper bounds on the stochastic convolution. We begin by deriving upper bounds on the maximum norm of the stochastic convolution. Rather than dealing directly with the solution of (4.2), we consider a slightly more general form of the stochastic convolution. In our setting of section 2, the noise process ξ is the generalized derivative of the Q-Wiener process W defined in (2.1), and the latter involves a sum over $\mathbb{N}^2$. For the convenience of the technical estimates in the present section, we would like to avoid the use of double indices, and therefore a general stochastic convolution written in the following form where $(k,l) \in \mathbb{N}^2$ is replaced by a $k \in \mathbb{N}^2$.

Definition 4.3. *Let $\Omega \subset \mathbb{R}^d$ denote a bounded domain with Lipschitz boundary. Then we consider a general* stochastic convolution *of the form*

$$W_A(t,x) = \sum_{k\in I} \alpha_k \cdot \int_0^t e^{\eta_k(t-s)}\, d\beta_k(s) \cdot \psi_k(x) \qquad \text{for} \quad t \geq 0\,, \quad x \in \Omega\,, \tag{4.3}$$

where $I \subset \mathbb{N}^d$ denotes an arbitrary index set. The functions $\psi_k : \Omega \to \mathbb{R}$ for $k \in I$ are pairwise orthogonal in the Hilbert space $L^2(\Omega)$. Moreover, the real constants $\eta_k \leq c < 0$ are strictly

negative for all $k \in I$ and uniformly bounded away from 0, and $\{\beta_k\}_{k\in I}$ denotes a family of independent real-valued standard Brownian motions over a common probability space $(F, \mathcal{F}, \mathbb{P})$. Finally, the positive coefficients $\alpha_k > 0$ for $k \in I$ measure the noise strength of the individual Fourier modes in the series representation (4.3).

While we delay a full comparison to our previous notation, for now recall that in section 2 we studied the two-dimensional case $d = 2$ with domain $\Omega = (0,1)^2$, and the eigenvalues η_k are given by (1.3), where μ in the nucleation region implies that $\eta_k < 0$. In fact, in the two-dimensional case the κ_k are the real numbers $\pi^2(j^2 + \ell^2)$ for $j, \ell \in \mathbb{N}_0$, and the corresponding eigenfunctions ψ_k are precisely the forcing modes $\varphi_{j,\ell}$ defined in (2.2). Finally, we assumed that the noise intensities satisfy $\alpha_k = 1$ on the index set I and are zero otherwise. For our simulations in section 2.1, the index set I describes a quarter ring in $\mathbb{N}_0^2$, while in section 2.2 we used an index set with $|I| = 1$.

We now turn to bounding the stochastic convolution W_A. As mentioned before, our upper bound is uniform in the space variable, i.e., with respect to the (spatial) maximum norm. Our approach is based on classical fractional Sobolev embedding results, and it will be used to obtain polynomial moments of W_A. This is necessary since due to the degeneracy of the driving noise we cannot directly employ the theory of large deviations. This approach has previously been used, for example, by Da Prato and Debussche [9], Blömker and Hairer [3], and Da Prato and Zabczyck [10]. We believe that by extending the method of Wanner [36] or Desi, Sander, and Wanner [12], both of which are based on results due to Kahane [22], it might be possible to improve our estimate by deriving exponential moments of the stochastic convolution. This in turn would lead to exponentially small probability estimates and therefore exponentially long time scales—albeit at the expense of a significantly more involved proof. However, the approach presented here is simple and direct and yields a result which is sufficient for our purposes. In the following, we need an additional assumption which constrains the growth of the eigenvalues η_k and the coefficients α_k.

Assumption 4.4. In the following, we assume that the function values $\psi_k(x)$ and the real numbers $|k|^{-1}\mathrm{Lip}(\psi_k)$ are uniformly bounded for $x \in \Omega$ and $k \in I$, where $\mathrm{Lip}(\psi)$ denotes the global Lipschitz constant of a function ψ. In addition, we assume that there is a small constant $\delta \in (0, 1/2)$ such that the estimate

$$S_\delta := \sum_{k\in I} \alpha_k^2 \cdot \frac{|\eta_k|^\delta + |k|^\delta + 1}{|\eta_k|} < \infty \tag{4.4}$$

holds.

Under our assumptions, if (4.4) holds for one $\delta > 0$, then it holds for all smaller δ, too. In the setting of section 2, where we consider only finite cosine sums, Assumption 4.4 is automatically satisfied for all $\delta > 0$, and moreover we can calculate S_δ explicitly.

Suppose now that we are in the situation of Definition 4.3 and that Assumption 4.4 is satisfied. In order to bound the stochastic convolution W_A uniformly with respect to both space and time, we use the Sobolev embedding theorem for the fractional Sobolev space $W^{\alpha,p}([0,T]\times\Omega)$,

which is defined for $\alpha \in (0,1)$ by the norm

$$\|w\|_{W^{\alpha,p}([0,T]\times\Omega)} = \Bigg(\int_0^T \int_\Omega |w(t,x)|^p \, dx\, dt + \int_0^T \int_0^T \int_\Omega \int_\Omega \frac{|w(t,x)-w(s,y)|^p}{(|x-y|+|t-s|)^{\alpha p+d+1}} \, dx\, dy\, dt\, ds\Bigg)^{1/p} \tag{4.5}$$

for all $w \in W^{\alpha,p}([0,T]\times\Omega)$, where d is the dimension of Ω. If we assume that $\alpha p > d+1$ holds, then this fractional Sobolev space can be embedded into the space $C^0([0,T]\times\overline{\Omega})$ according to [30, Theorem 1, section 2.2.4]; see also [30, section 2.4.4]. Notice, however, that the resulting embedding constant will depend on the underlying domain size, and therefore on T.

To circumvent this T-dependence, we apply the Sobolev embedding theorem not to realizations of the stochastic convolution $W_A(\cdot,\cdot)$, but rather to realizations of the rescaled process $W_A(T\cdot,\cdot)$, where now the time argument is taken from the unit interval $[0,1]$. That is, there exists a T-independent constant $C>0$ such that

$$\begin{aligned}\sup_{t\in[0,T]}\sup_{x\in\Omega}|W_A(t,x)|^p &= \sup_{t\in[0,1]}\sup_{x\in\Omega}|W_A(Tt,x)|^p \;\le\; C\|W_A(T\cdot,\cdot)\|^p_{W^{\alpha,p}([0,1]\times\Omega)} \\ &= \frac{C}{T^2}\int_0^T\int_0^T\int_\Omega\int_\Omega \frac{|W_A(t,x)-W_A(s,y)|^p}{(|x-y|+|t-s|/T)^{\alpha p+d+1}}\,dx\,dy\,dt\,ds \\ &\quad + \frac{C}{T}\int_0^T\int_\Omega |W_A(t,x)|^p\,dx\,dt\,.\end{aligned}$$

If $T \ge 1$, then we further have

$$\begin{aligned}&\int_0^T\int_0^T\int_\Omega\int_\Omega \frac{|W_A(t,x)-W_A(s,y)|^p}{(|x-y|+|t-s|/T)^{\alpha p+d+1}}\,dx\,dy\,dt\,ds \\ &\quad= T^{\alpha p+d+1}\int_0^T\int_0^T\int_\Omega\int_\Omega \frac{|W_A(t,x)-W_A(s,y)|^p}{(|x-y|T+|t-s|)^{\alpha p+d+1}}\,dx\,dy\,dt\,ds \\ &\quad\le T^{\alpha p+d+1}\int_0^T\int_0^T\int_\Omega\int_\Omega \frac{|W_A(t,x)-W_A(s,y)|^p}{(|x-y|+|t-s|)^{\alpha p+d+1}}\,dx\,dy\,dt\,ds\,,\end{aligned}$$

while for $T \le 1$ one obtains

$$\begin{aligned}&\int_0^T\int_0^T\int_\Omega\int_\Omega \frac{|W_A(t,x)-W_A(s,y)|^p}{(|x-y|+|t-s|/T)^{\alpha p+d+1}}\,dx\,dy\,dt\,ds \\ &\quad\le \int_0^T\int_0^T\int_\Omega\int_\Omega \frac{|W_A(t,x)-W_A(s,y)|^p}{(|x-y|+|t-s|)^{\alpha p+d+1}}\,dx\,dy\,dt\,ds\,.\end{aligned}$$

Combined, these inequalities furnish the estimate

$$\sup_{t\in[0,T]}\sup_{x\in\Omega}|W_A(t,x)|^p \;\leq\; \frac{C}{T}\int_0^T\int_\Omega |W_A(t,x)|^p\,dx\,dt + \frac{C\left(T^{\alpha p+d+1}+1\right)}{T^2}\int_0^T\int_0^T\int_\Omega\int_\Omega \frac{|W_A(t,x)-W_A(s,y)|^p}{(|x-y|+|t-s|)^{\alpha p+d+1}}\,dx\,dy\,dt\,ds \tag{4.6}$$

for every realization of the stochastic convolution W_A, as long as the norm on the right-hand side is finite, where the constant C does not depend on T. Based on this, we introduce the convention that from now on, the constant C denotes a generic positive constant, whose value can change from line to line, and which might depend on Ω, on the uniform bounds for the ψ_k, on α, or on p, but which does not depend on the time T. Note that the constants α and p will be fixed later.

We continue our estimates by first providing a bound on the expectation of the right-hand side of (4.6). To this end, throughout our discussion we use the choice

$$\alpha := \frac{2(d+1)}{p}\,, \tag{4.7}$$

which implies that the Sobolev embedding always holds, and we think of p as being a very large number. In order to bound the expected value of the double integral in the first line of (4.6), we use the independence of the Fourier components, the fact that the expectation of stochastic integrals vanishes, and Itô's isometry to derive the identity

$$\begin{aligned}\mathbb{E}\,|W_A(t,x)|^2 &= \sum_{k\in I}\alpha_k^2\cdot\mathbb{E}\left(\int_0^t e^{\eta_k(t-s)}d\beta_k(s)\right)^2\cdot|\psi_k(x)|^2\\ &= \sum_{k\in I}\alpha_k^2\cdot\int_0^t e^{2\eta_k(t-s)}ds\cdot|\psi_k(x)|^2 \;\leq\; C\sum_{k\in I}\frac{\alpha_k^2}{|\eta_k|} \;\leq\; CS_\delta\,.\end{aligned}$$

For every fixed $t\geq 0$ and all $x\in\Omega$ the real-valued random variable $W_A(t,x)$ is a centered Gaussian variable: This is clearly satisfied if the index set I is finite, since in this case $W_A(t,x)$ is a sum of independent Gaussian random variables. In the case of infinite index set I, one can derive an estimate similar to the one which establishes the convergence of the sum (4.3) in mean square with respect to the expectation $\mathbb{E}$.

Gaussianity then implies that the pth moment is always bounded by the second, and thus we obtain the estimate

$$\int_0^T\int_\Omega \mathbb{E}\,|W_A(t,x)|^p\,dx\,dt \;\leq\; \int_0^T\int_\Omega\left(\mathbb{E}\,|W_A(t,x)|^2\right)^{p/2}dx\,dt \;\leq\; CTS_\delta^{p/2}\,. \tag{4.8}$$

We now turn our attention to the expectation of the quadruple integral in the second line of estimate (4.6). Also, in this case, we begin by applying independence and the Itô isometry, which implies

$$\mathbb{E}\,|W_A(t,x)-W_A(t,y)|^2 \;=\; \sum_{k\in I}\frac{\alpha_k^2}{2|\eta_k|}\left(1-e^{2t\eta_k}\right)|\psi_k(x)-\psi_k(y)|^2\;.$$

Notice that again, for fixed $t \geq 0$ and $x, y \in \Omega$, the difference $W_A(t,x) - W_A(t,y)$ is a well-defined real-valued Gaussian random variable. According to Assumption 4.4, the functions ψ_k are uniformly bounded, and for every small value of $\delta \in (0,2)$ there exists a constant C such that

$$|\psi_k(x) - \psi_k(y)|^2 \;\leq\; C\,|\psi_k(x) - \psi_k(y)|^\delta \;\leq\; C|k|^\delta |x-y|^\delta \,,$$

where we use the bound on the Lipschitz-constant, as well as the uniform boundedness of the ψ_k. Combining both of the previous estimates now yields

$$\mathbb{E}\,|W_A(t,x) - W_A(t,y)|^2 \;\leq\; C \sum_{k\in I} \frac{\alpha_k^2}{|\eta_k|} |k|^\delta |x-y|^\delta \;\leq\; C S_\delta |x-y|^\delta \,. \tag{4.9}$$

So far we have only considered differences of the form $|W_A(t,x) - W_A(t,y)|$, i.e., differences where the time arguments coincide and the spatial arguments differ. Now we consider the opposite case, i.e., differences of the form $|W_A(t,x) - W_A(s,x)|$. Without loss of generality we assume that $t > s$. Then the independence of increments of a Brownian motion and Itô's isometry imply the identity

$$\begin{aligned}
&\mathbb{E}\left(\int_0^t e^{\eta_k(t-\tau)}\,d\beta_k(\tau) - \int_0^s e^{\eta_k(s-\tau)}\,d\beta_k(\tau)\right)^2 \\
&\quad= \mathbb{E}\left(\int_0^s \left(e^{\eta_k(t-\tau)} - e^{\eta_k(s-\tau)}\right) d\beta_k(\tau)\right)^2 + \mathbb{E}\left(\int_s^t e^{\eta_k(t-\tau)}\,d\beta_k(\tau)\right)^2 \\
&\quad= \int_0^s \left(e^{\eta_k t} - e^{\eta_k s}\right)^2 e^{-2\eta_k \tau}\,d\tau + \int_s^t e^{2\eta_k(t-\tau)}\,d\tau \\
&\quad= \frac{1}{2|\eta_k|}\left(e^{\eta_k t} - e^{\eta_k s}\right)^2 \left(e^{-2\eta_k s} - 1\right) + \frac{1}{2|\eta_k|}\left(1 - e^{2\eta_k(t-s)}\right) .
\end{aligned}$$

Now we proceed by using the fact that exponential terms are bounded by one due to $\eta_k < 0$, together with the estimate that for $x \geq 0$ one has $|1 - e^{-x}| \leq |x|$, which follows easily from the mean value theorem. For every value of $\delta \in (0,1)$, one obtains

$$\begin{aligned}
&\mathbb{E}\left(\int_0^t e^{\eta_k(t-\tau)}\,d\beta_k(\tau) - \int_0^s e^{\eta_k(s-\tau)}\,d\beta_k(\tau)\right)^2 \\
&\quad\leq \frac{1}{2|\eta_k|}\left(e^{\eta_k(t-s)} - 1\right)^2 + \frac{1}{2|\eta_k|}\left(1 - e^{2\eta_k(t-s)}\right) \\
&\quad\leq \frac{1}{2|\eta_k|}\left|e^{\eta_k(t-s)} - 1\right|^\delta + \frac{1}{2|\eta_k|}\left|1 - e^{2\eta_k(t-s)}\right|^\delta \\
&\quad\leq \frac{C}{|\eta_k|}\,|\eta_k|^\delta\,|t-s|^\delta \,,
\end{aligned}$$

where the constant C depends on δ, which in turn will be fixed later. Together with the definition of the stochastic convolution in (4.3), the fact that the $|\eta_k|$ are uniformly bounded

away from zero, and the uniform boundedness of the functions ψ_k, this yields

$$\begin{aligned}
&\mathbb{E}\,|W_A(t,x) - W_A(s,x)|^2 \\
&\qquad \leq\ C \sum_{k\in I} \alpha_k^2 \cdot \mathbb{E}\left(\int_0^t e^{\eta_k (t-\tau)}\, d\beta_k(\tau) - \int_0^s e^{\eta_k (s-\tau)}\, d\beta_k(\tau) \right)^2 |\psi_k(x)|^2 \\
&\qquad \leq\ C \sum_{k\in I} \frac{\alpha_k^2}{|\eta_k|}\, |\eta_k|^\delta\, |t-s|^\delta \ \leq\ C S_\delta |t-s|^\delta\,. \qquad (4.10)
\end{aligned}$$

Combining (4.9) and (4.10) finally implies the estimate

$$\mathbb{E}\,|W_A(t,x) - W_A(s,y)|^2 \ \leq\ C S_\delta \left(|t-s| + |x-y|\right)^\delta\,, \qquad (4.11)$$

where S_δ was introduced in Assumption 4.4. Before the next estimate, we fix a particular choice of δ as follows:

$$\delta := 3\alpha = \frac{6(d+1)}{p}\,. \qquad (4.12)$$

Due to (4.7), this choice of δ implies

$$(\delta/2 - \alpha)p - d - 1 = 0. \qquad (4.13)$$

Note that as long as p is chosen to be sufficiently large, the choice of δ in (4.12) can be made sufficiently small so that Assumption 4.4 is satisfied.

With our choice of δ made, we are now in a position to obtain an estimate for the expected value of the quadruple integral in the second line of (4.6). Using Fubini's theorem, the Gaussianity of the difference $W_A(t,x) - W_A(s,y)$, and (4.13), one obtains

$$\begin{aligned}
&\mathbb{E} \int_0^T \int_0^T \int_\Omega \int_\Omega \frac{|W_A(t,x) - W_A(s,y)|^p}{(|x-y| + |t-s|)^{\alpha p + d + 1}}\, dx\, dy\, dt\, ds \\
&\qquad \leq\ C S_\delta^{p/2} \int_0^T \int_0^T \int_\Omega \int_\Omega (|x-y| + |t-s|)^{(\delta/2-\alpha)p - d - 1}\, dx\, dy\, dt\, ds \\
&\qquad \leq\ C S_\delta^{p/2} T^2\,. \qquad (4.14)
\end{aligned}$$

We now return to our initial Sobolev embedding estimate (4.6). In preparation, we note that according to (4.7) we have $\alpha p + d + 1 = 3(d+1)$. Taking expectations on both sides and applying the estimates in (4.8) and (4.14) finally implies the existence of a T-independent constant $C > 0$ such that

$$\mathbb{E} \sup_{t\in[0,T]} \sup_{x\in\Omega} |W_A(t,x)|^p \ \leq\ C S_\delta^{p/2} \left(T^{\alpha p + d + 1} + 1 \right) \ =\ C S_\delta^{p/2} \left(T^{3(d+1)} + 1 \right) \quad \text{for all} \quad T \geq 0\,.$$

Now let $1 < q \leq p$ be arbitrary. Then Hölder's inequality applied to random variables over $(F, \mathcal{F}, \mathbb{P})$ implies for all $T \geq 1$ the estimates

$$\mathbb{E} \sup_{t\in[0,T]} \sup_{x\in\Omega} |W_A(t,x)|^q \;\leq\; \Big(\mathbb{E} \sup_{t\in[0,T]} \sup_{x\in\Omega} |W_A(t,x)|^p\Big)^{q/p} \;\leq\; C^{q/p} S_\delta^{q/2} T^{3(d+1)q/p} \,,$$

and by choosing p sufficiently large, this finally furnishes the following theorem, where we replaced q again by p.

Theorem 4.5. *Consider the stochastic convolution W_A introduced in Definition 4.3, and suppose that Assumption 4.4 holds. Then for arbitrary constants $\gamma > 0$ and all $p > 1$ there exists a constant $C > 0$ such that*

$$\mathbb{E} \sup_{t\in[0,T]} \sup_{x\in\Omega} |W_A(t,x)|^p \;\leq\; C S_\delta^{p/2} T^\gamma \qquad \text{for all} \qquad T \geq 1 \,,$$

where the constant S_δ was defined in (4.4).

With the above estimate, Chebyshev's inequality finally implies that for all large $p > 1$ and all small $\gamma > 0$ there exists a constant $C > 0$ which depends on p and γ such that for all threshold values $\theta > 0$ and constants $\sigma > 0$, we have

$$\mathbb{P}\Big(\sup_{t\in[0,T]} \sigma \, \|W_A(t,\cdot)\|_{L^\infty(\Omega)} \;\geq\; \theta \Big) \;\leq\; C\, T^\gamma \, \big(\sigma^2 S_\delta\big)^{p/2} \, \theta^{-p} \quad \text{for all} \quad T \geq 1 \,,$$

where the constant σ should be interpreted as the noise intensity of our stochastic process. Thus, if the value of the product $\sigma^2 S_\delta \ll 1$ is small, then on large time intervals $[0, T]$ the probability that the stochastic convolution is small turns out to be close to one. In other words, nucleation cannot occur on such time intervals unless the strength of the noise is very large. In other words, if $\Upsilon \ll 1$ is a fixed probability tolerance, then we have for all large $p > 1$ and small $\gamma > 0$ a with constant $C > 0$ depending on p and γ

$$\mathbb{P}\Big(\sup_{t\in[0,T]} \sigma \, \|W_A(t,\cdot)\|_{L^\infty(\Omega)} \;<\; \theta \Big) \;\geq\; 1 - \Upsilon \quad \text{as long as} \quad 1 \;\leq\; T \;\leq\; C\, \Upsilon^{1/\gamma} \left(\frac{\theta^2}{\sigma^2 S_\delta} \right)^{p/2\gamma} .$$

Clearly the expression on the right varies as a positive power of the inverse noise strength $1/\sigma$; i.e., nucleation cannot occur on time intervals whose length is of this order.

Note that the asymptotic regime in Example 4.2 corresponds to our numerical simulations if we choose $\tau = \varrho = 0$, which is exactly the regime in which we cannot exclude nucleation on large time frames. Finally, we also see that nucleation is more unlikely for larger values of r_0, as in this case S_δ becomes very small. But in our numerical simulations, we did not study a very large range of r_0, and thus this effect did not show up. Moreover, for excessively large values of r_0 the carrying capacity of the domain was too small to sustain nucleation, and even quite large values of the stochastic convolution W_A would not trigger the spontaneous formation of nucleii.

4.2. Lower bounds on the maximum norm. For the lower bound on the stochastic convolution, we give a straightforward argument which already solves the problem in our setting; see also Example 4.2. Note, however, that one should be able to obtain much finer estimates

by using more sophisticated methods for Gaussian processes. In our setting, we need the following assumption.

Assumption 4.6. Consider the stochastic convolution W_A introduced in Definition 4.3 and (4.3). We assume that there exists a point $x_* \in \Omega$ such that $\psi_k(x_*) = 1$ for all $k \in I$.

Note that in the case of the domain $\Omega = (0, L)^2$ and homogeneous Neumann boundary conditions, this is satisfied with $x_* = 0$.

Now define $Z_k(t) = \int_0^t e^{\eta_k(t-s)}\, d\beta_k(s)$ and $\alpha_k = 1$ for all $k \in I$. Then Assumption 4.6 immediately implies

$$W_A(t, x_*) = \sum_{k\in I} Z_k(t) \quad \text{for all} \quad t \geq 0\,.$$

Due to the definition of the maximum and elementary probability theory, one then obtains

$$\mathbb{P}\Big(\sup_{t\in[0,T]} \|\sigma W_A(t,\cdot)\|_{L^\infty(\Omega)} \leq \theta \Big) \;\leq\; \mathbb{P}\Big(|\sigma W_A(T, x_*)| \leq \theta \Big)\,.$$

Since $W_A(T, x_*)$ is in fact a centered real-valued Gaussian random variable with variance

$$\Sigma_T^2 \;=\; \sum_{k\in I} \mathbb{E} Z_k(T)^2 \;=\; \sum_{k\in I} \frac{1 - e^{2T\eta_k}}{2\,|\eta_k|}\,,$$

we can bound the Gaussian density by its maximum value to further obtain

$$\mathbb{P}\Big(\sup_{t\in[0,T]} \|\sigma W_A(t,\cdot)\|_{L^\infty(\Omega)} \leq \theta \Big) \;\leq\; \frac{1}{\sqrt{2\pi}\cdot\sigma\Sigma_T} \int_{-\theta}^{\theta} e^{-s^2/(2\sigma^2\Sigma_T^2)}\, ds \;\leq\; \frac{2\theta}{\sqrt{2\pi}\cdot\sigma\Sigma_T}\,.$$

Notice that we have $\Sigma_T \approx S_0$ for $T \gg \max\{1/|\eta_k| \,:\, k \in I\}$. This implies that in the situation of Example 4.2 solutions become large over the time interval $[0, T]$ with high probability, as long as the noise strength σ is much larger than $1/S_0$. For this to hold, the time frame is given by the relatively small time value $T \sim r_0^{-2}$ or $T \sim r_0^{-4}\varepsilon^{-2}$, depending on whether we have $1 < r_0 < 1/\varepsilon$ or $r_0 > 1/\varepsilon$, respectively. Note that in these two cases we have $\varepsilon^2 < T < 1$ or $T < \varepsilon^2$, respectively. Moreover, the necessary noise level is not considerably bigger than the threshold $1/S_\delta$ below which no nucleation can be observed on very long time-scales. These observations were summarized in the beginning of the section. We state these findings again, this time with our rigorous bounds developed in the section.

Observation 4.7 (solution size for the linearized problem). Consider the stochastic convolution W_A, which solves the linearized Cahn–Hilliard–Cook problem (4.2). Then the following holds, where S_δ was introduced in Assumption 4.4.

- For noise strengths σ much smaller than $1/S_\delta$ the solutions of the linearized Cahn–Hilliard–Cook model (4.2) in the nucleation regime stay small over very large time intervals, which are almost of exponential size.
- For noise strengths σ much larger than $1/S_0$, and after relatively short times of order $\max\{1/|\eta_k| \,:\, k \in I\}$, the solutions of the linearized Cahn–Hilliard–Cook model become large with high probability.

We would like to point out that while S_0 is smaller than S_δ, one does have $S_\delta \to S_0$ as $\delta \to 0$.

Remark 4.8 (large values of W_A do not guarantee nucleation). The results of this section show that the solution of the linearized problem is likely to be large after relatively small

times. Note, however, that as we have already seen, this does not guarantee nucleation. See, for example, the large noisy fluctuations in the last two pictures of Figure 2. In these cases the stochastic convolution W_A is large, yet nuclei are not really observed. If we would increase the radius r_0 in that figure even further, then we would not see any nuclei, but only the (very large) background noise.

We close this analytical section with a brief remark concerning rigorous bounds for the nonlinear problem (1.4). Based on the linear results above, one can derive nonlinear bounds in a straightforward, albeit very technical, manner. Such results involve using the mild solution of the nonlinear problem which is defined via the variation of constants formula, as well as bounds of the form $\|e^{tA}\Delta w\|_\infty \leq Ct^{-1/2}\|w\|_\infty$ for the linearized Cahn–Hilliard operator A. Estimates of this type can be obtained using the Green's functions–based approach discussed in [7, 29]. However, since in our setting we are only interested in small amplitude solutions, the cubic term can be rigorously estimated and shown to be much smaller.

5. Conclusions. In this paper, we studied a two-dimensional stochastic Cahn–Hilliard–Cook equation in the nucleation regime in the case of degenerate noise. We used direct simulations to show that if the noise is band-limited in its spatial frequency, a high frequency noise results in a complete loss of pattern formation at the forced length scale, instead leading to the delayed formation of nuclei with larger sizes. We then used numerical continuation methods to show that there is a minimum domain size required to sustain a droplet. Too high a spatial frequency forces a small local domain size, resulting in the above loss of the specifically forced nucleation pattern. Finally, we used rigorous probabilistic methods on the linearized equation to give the expected time of nucleation with respect to the amplitude and spatial frequency of the degenerate noise.

To the best of our knowledge, this is the first numerical study of degenerate noise for nucleation for the Cahn–Hilliard equation. We are able to understand the droplet structure seen (and not seen) based on numerical continuation. Our numerics have uncovered many interesting questions for future research. For example, we would also like to develop a better understanding of our observed scaling laws, as well as to understand how multiple modes interact. Furthermore, preliminary numerical simulations for periodic boundary conditions gave a completely different set of behaviors; we would like to understand why, though one barrier to fully repeating the numerical methods shown here is that due to symmetry, continuation methods for periodic boundary conditions are trickier than for Neumann boundary conditions. In the long term, we hope to consider our results in the context of importance sampling to see if they allow us to draw conclusions in the context of space-time white noise. Many of the results in this paper are numerical in nature, and many of the statements may be intractable in terms of traditional handwritten proofs. We propose instead verifying numerical results through the use of rigorous computational techniques.

REFERENCES

[1] P. W. Bates and P. C. Fife, *The dynamics of nucleation for the Cahn–Hilliard equation*, SIAM J. Appl. Math., 53 (1993), pp. 990–1008.

[2] D. Blömker, B. Gawron, and T. Wanner, *Nucleation in the one-dimensional stochastic Cahn-Hilliard model*, Discrete Contin. Dyn. Syst., 27 (2010), pp. 25–52.

[3] D. Blömker and M. Hairer, *Multiscale expansion of invariant measures for SPDEs*, Comm. Math. Phys., 251 (2004), pp. 515–555.
[4] D. Blömker, S. Maier-Paape, and T. Wanner, *Spinodal decomposition for the Cahn-Hilliard-Cook equation*, Comm. Math. Phys., 223 (2001), pp. 553–582.
[5] D. Blömker, S. Maier-Paape, and T. Wanner, *Phase separation in stochastic Cahn-Hilliard models*, in Mathematical Methods and Models in Phase Transitions, A. Miranville, ed., Nova Science Publishers, New York, 2005, pp. 1–41.
[6] D. Blömker, S. Maier-Paape, and T. Wanner, *Second phase spinodal decomposition for the Cahn-Hilliard-Cook equation*, Trans. Amer. Math. Soc., 360 (2008), pp. 449–489.
[7] P. Collet and J.-P. Eckmann, *The time dependent amplitude equation for the Swift-Hohenberg problem*, Comm. Math. Phys., 132 (1990), pp. 139–153.
[8] H. Cook, *Brownian motion in spinodal decomposition*, Acta Metallurgica, 18 (1970), pp. 297–306.
[9] G. Da Prato and A. Debussche, *Stochastic Cahn-Hilliard equation*, Nonlinear Anal., 26 (1996), pp. 241–263.
[10] G. Da Prato and J. Zabczyk, *Stochastic Equations in Infinite Dimensions*, 2nd ed., Cambridge University Press, Cambridge, UK, 2014.
[11] J. P. Desi, H. H. Edrees, J. J. Price, E. Sander, and T. Wanner, *The dynamics of nucleation in stochastic Cahn–Morral systems*, SIAM J. Appl. Dyn. Syst., 10 (2011), pp. 707–743.
[12] J. P. Desi, E. Sander, and T. Wanner, *Complex transient patterns on the disk*, Discrete Contin. Dyn. Syst., 15 (2006), pp. 1049–1078.
[13] E. Doedel, *AUTO: A program for the automatic bifurcation analysis of autonomous systems*, in Proceedings of the Tenth Manitoba Conference on Numerical Mathematics and Computing, Vol. I (Winnipeg, Man., CA, 1980), Congr. Numer., 30 (1981), pp. 265–284.
[14] M. Gameiro, K. Mischaikow, and T. Wanner, *Evolution of pattern complexity in the Cahn-Hilliard theory of phase separation*, Acta Materialia, 53 (2005), pp. 693–704.
[15] L. Goudenège and L. Manca, *Asymptotic properties of stochastic Cahn-Hilliard equation with singular nonlinearity and degenerate noise*, Stochastic Process. Appl., 125 (2015), pp. 3657–4020.
[16] M. Grinfeld and A. Novick-Cohen, *The viscous Cahn-Hilliard equation: Morse decomposition and structure of the global attractor*, Trans. Amer. Math. Soc., 351 (1999), pp. 2375–2406.
[17] M. Hairer and J. C. Mattingly, *Ergodicity of the 2D Navier-Stokes equations with degenerate stochastic forcing*, Ann. of Math. (2), 164 (2006), pp. 993–1032.
[18] M. Hairer and J. C. Mattingly, *Spectral gaps in Wasserstein distances and the 2D stochastic Navier-Stokes equations*, Ann. Probab., 36 (2008), pp. 2050–2091.
[19] T. Hartley and T. Wanner, *A semi-implicit spectral method for stochastic nonlocal phase-field models*, Discrete Contin. Dyn. Syst., 25 (2009), pp. 399–429.
[20] P. C. Hohenberg and B. I. Halperin, *Theory of dynamic critical phenomena*, Rev. Modern Phys., 49 (1977), pp. 435–479.
[21] I. Johnson, E. Sander, and T. Wanner, *Branch interactions and long-term dynamics for the diblock copolymer model in one dimension*, Discrete Contin. Dyn. Syst., 33 (2013), pp. 3671–3705.
[22] J.-P. Kahane, *Some Random Series of Functions*, 2nd ed., Cambridge University Press, Cambridge, UK, 1985.
[23] J. S. Langer, *Theory of spinodal decomposition in alloys*, Ann. Phys., 65 (1971), pp. 53–86.
[24] S. Maier-Paape, U. Miller, K. Mischaikow, and T. Wanner, *Rigorous numerics for the Cahn-Hilliard equation on the unit square*, Rev. Mat. Complut., 21 (2008), pp. 351–426.
[25] S. Maier-Paape, K. Mischaikow, and T. Wanner, *Structure of the attractor of the Cahn-Hilliard equation on a square*, Internat. J. Bifur. Chaos Appl. Sci. Engrg., 17 (2007), pp. 1221–1263.
[26] S. Maier-Paape and T. Wanner, *Spinodal decomposition for the Cahn-Hilliard equation in higher dimensions. Part* I: *Probability and wavelength estimate*, Comm. Math. Phys., 195 (1998), pp. 435–464.
[27] S. Maier-Paape and T. Wanner, *Spinodal decomposition for the Cahn-Hilliard equation in higher dimensions: Nonlinear dynamics*, Arch. Ration. Mech. Anal., 151 (2000), pp. 187–219.
[28] K. Mischaikow, *Global asymptotic dynamics of gradient-like bistable equations*, SIAM J. Math. Anal., 26 (1995), pp. 1199–1224.

[29] W. W. Mohammed, D. Blömker, and K. Klepel, *Modulation equation for stochastic Swift–Hohenberg equation*, SIAM J. Math. Anal., 45 (2013), pp. 14–30.
[30] T. Runst and W. Sickel, *Sobolev Spaces of Fractional Order, Nemytskij Operators, and Nonlinear Partial Differential Equations*, Walter de Gruyter, Berlin, 1996.
[31] E. Sander and T. Wanner, *Monte Carlo simulations for spinodal decomposition*, J. Statist. Phys., 95 (1999), pp. 925–948.
[32] E. Sander and T. Wanner, *Unexpectedly linear behavior for the Cahn–Hilliard equation*, SIAM J. Appl. Math., 60 (2000), pp. 2182–2202.
[33] R. Temam, *Infinite-Dimensional Dynamical Systems in Mechanics and Physics*, 2nd ed., Springer-Verlag, New York, 1997.
[34] J. D. van der Waals, *The thermodynamic theory of capillarity flow under the hypothesis of a continuous variation in density*, Verh. Konink. Akad. Wetensch. Amsterdam, 1 (1893), pp. 1–56.
[35] E. Vanden-Eijnden and M. G. Westdickenberg, *Rare events in stochastic partial differential equations on large spatial domains*, J. Statist. Phys., 131 (2008), pp. 1023–1038.
[36] T. Wanner, *Maximum norms of random sums and transient pattern formation*, Trans. Amer. Math. Soc., 356 (2004), pp. 2251–2279.
[37] T. Wanner, *Computer-assisted equilibrium validation for the diblock copolymer model*, Discrete Contin. Dyn. Syst., to appear.
[38] T. Wanner, *Topological analysis of the diblock copolymer equation*, in Mathematical Challenge to a New Phase of Materials Science, Springer Proc. Math. Statist., K. Obuse, Y. Nishiura, and N. Yoshinaga, eds., Springer-Verlag, Berlin, to appear.